

The XMM Cluster Outskirts Project (X-COP): Thermodynamic properties of the Intracluster Medium out to R_{200} in Abell 2319

V. Ghirardini^{1,2}, S. Ettori^{2,3}, D. Eckert^{4,5}, S. Molendi⁶, F. Gastaldello⁶, E. Pointecouteau^{7,8}, G. Hurier^{9,10}, H. Bourdin^{11,12}

¹ Dipartimento di Fisica e Astronomia Università di Bologna, Via Piero Gobetti, 93/2, 40129 Bologna, Italy

² INAF, Osservatorio Astronomico di Bologna, Via Piero Gobetti, 93/3, 40129 Bologna, Italy

³ INFN, Sezione di Bologna, viale Berti Pichat 6/2, 40127 Bologna, Italy

⁴ Max-Planck Institut für Extraterrestrisch Physik, Giessenbachstrasse 1, 85748 Garching, Germany

⁵ Department of Astronomy, University of Geneva, ch. d'Ecogia 16, 1290 Versoix, Switzerland

⁶ INAF - IASF-Milano, Via E. Bassini 15, 20133 Milano, Italy

⁷ CNRS; IRAP; 9 Av. colonel Roche, BP 44346, F-31028 Toulouse cedex 4, France

⁸ Université de Toulouse; UPS-OMP; IRAP; Toulouse, France

⁹ Centro de Estudios de Física del Cosmos de Aragon, Plaza San Juan 1, Planta-2, 44001, Teruel, Spain

¹⁰ Institut d'Astrophysique Spatiale, CNRS (UMR8617) Université Paris-Sud 11, Batiment 121, Orsay, France

¹¹ Harvard Smithsonian Centre for Astrophysics, 60 Garden Street, Cambridge, MA 02138, USA

¹² Dipartimento di Fisica, Università degli Studi di Roma Tor Vergata, via della Ricerca Scientifica, 1, I-00133 Roma, Italy

January 22, 2018

ABSTRACT

Aims. We present the joint analysis of the X-ray and Sunyaev-Zeldovich signals in Abell 2319, the galaxy cluster with the highest signal-to-noise ratio in SZ *Planck* maps and that has been surveyed within our *XMM-Newton* Cluster Outskirts Project (X-COP), a very large program which aims to grasp the physical condition in 12 local ($z < 0.1$) and massive ($M_{200} > 3 \times 10^{14} M_{\odot}$) galaxy clusters out to R_{200} and beyond.

Methods. We recover the profiles of the thermodynamic properties by the geometrical deprojection of the X-ray surface brightness, of the SZ comptonization parameter, and accurate and robust spectroscopic measurements of the gas temperature, out to 3.2 Mpc ($1.6 R_{200}$), 4 Mpc ($2 R_{200}$), and 1.6 Mpc ($0.8 R_{200}$), respectively. We resolve the clumpiness of the gas density to be below 20 per cent over the entire observed volume. We also demonstrate that most of this clumpiness originates from the ongoing merger and can be associated to large-scale inhomogeneities (the “residual” clumpiness). We estimate the total mass through the hydrostatic equilibrium equation. This analysis is done both in azimuthally averaged radial bins and in eight independent angular sectors, enabling us to study in details the azimuthal variance of the recovered properties.

Results. Given the exquisite quality of the X-ray and SZ datasets, their radial extension and their complementarity, we constrain at R_{200} the total hydrostatic mass, modelled with a Navarro-Frenk-White profile, with very high precision ($M_{200} = 10.7 \pm 0.5^{\text{stat}} \pm 0.9^{\text{sys}} \times 10^{14} M_{\odot}$). We identify the on-going merger and how it is affecting differently the gas properties in the resolved azimuthal sectors. We have several indications that the merger has injected a high level of non-thermal pressure in this system: the clumping free density profile is above the average profile obtained by stacking Rosat/PSPC observations; the gas mass fraction recovered using our hydrostatic mass profile exceeds the expected cosmic gas fraction beyond R_{500} ; the pressure profile is flatter than the fit obtained by the *Planck* collaboration; the entropy profile is flatter than the mean one predicted from non-radiative simulations; the analysis in azimuthal sectors has revealed that these deviations occur in a preferred region of the cluster. All these tensions are resolved by requiring a relative support of about 40 per cent from non-thermal to the total pressure at R_{200} .

Key words. Galaxies: clusters: intracluster medium – Galaxies: clusters: general – X-rays: galaxies: clusters – (Galaxies:) intergalactic medium

1. Introduction

Cosmic structures evolve hierarchically from the primordial density fluctuations into larger and larger systems under the action of gravity. Galaxy clusters are the largest bound structures of the universe and the most recent products of structure formation. Baryons fall into the gravitational potential of dark matter halos and heat up to a temperature of the order of few millions Kelvin, emitting in X-rays mostly through *bremstrahlung* process. In the last few years our knowledge on the physical condition of the intra cluster medium (ICM) has significantly improved through the study of the Sunyaev-Zel'dovich effect (SZ; Sunyaev & Zeldovich 1972). It arises when cosmic microwave

background photons (CMB) are scattered by the free electrons of the ICM. The observed distortion of the CMB spectrum is directly proportional to the thermal electronic pressure integrated along the line of sight. This linear dependence implies that the SZ signal decreases more slowly than the X-ray signal, which depends quadratically on the density. The assumption that the ICM is fully thermalized and in hydrostatic equilibrium is usually made in several studies (see Ettori et al. 2013, for a review). However this assumption might not be valid in cluster outskirts, where the relative contribution of non-thermal pressure to the total one might not be negligible (e.g. Battaglia et al. 2012).

The matter distribution in the outskirts of galaxy clusters is expected to be clumpy (Nagai & Lau 2011; Vazza et al. 2013) and asymmetric (Eckert et al. 2012; Roncarelli et al. 2013), with substantial contribution from non-thermal physics, like turbulence and bulk motion (Vazza et al. 2011), cosmic rays (Pfrommer et al. 2007), and magnetic fields (Dolag et al. 1999). Gas clumping plays an important role in the outer parts of galaxy clusters. Zhuravleva et al. (2013) showed that the density distribution inside a given shell surrounding the cluster center can be described by a log-normal distribution modified by the presence of a high density tail produced by the presence of clumps. It was shown that the median of this distribution coincides with the mode of the log-normal, while the mean is biased high due to the presence of clumps. Observationally Eckert et al. (2015) have confirmed this result: they concluded that the median method is able to recover the true gas density profile when inhomogeneities are present.

The XMM cluster outskirts project (X-COP; Eckert et al. 2017) is a very large programme on *XMM-Newton* which aims to increase significantly our knowledge on the physical conditions in the outskirts of galaxy clusters. Thirteen local and massive systems have been selected on the basis of their high signal-to-noise ratio (SNR) in the *Planck* survey, and reported in the first catalog (Planck Collaboration et al. 2014).

In this paper, we focus on Abell 2319, the most significant SZ detection in the first *Planck* catalog, with a SNR of 49.0 in the second *Planck* catalog (Planck Collaboration et al. 2016b). Abell 2319 is a very hot and massive cluster at low redshift ($z=0.0557$; Struble & Rood 1999). Its galaxy distribution indicates this is a merger of two main components with a 3:1 mass ratio, the smaller system being located $10'$ north of the main structure (Oegerle et al. 1995). The cluster exhibits a prominent cold front SE of the main core (Ghizzardi et al. 2010) and a giant radio halo (Farnsworth et al. 2013; Storm et al. 2015).

The paper is organised as follows: in Section 2, we describe the reduction and analysis of X-ray data, from background modeling to spatial and spectral analysis; in Section 3, we present the data reduction and analysis of the *Planck* SZ data; in Section 4, we show the reconstructed profiles of the thermodynamic quantities, describe their properties, and discuss the different methods adopted to solve the hydrostatic equilibrium equation; in Section 5, the analysis in azimuthal sectors is illustrated. The gas mass fraction and the hydrostatic bias are shown in Section 6. The summary of our main findings and our conclusions are discussed in Section 7.

Throughout this paper, we assume a Λ CDM cosmology with $\Omega_\Lambda = 0.7$, $\Omega_m = 0.3$ and $H_0 = 70$ km/s/Mpc, $E(z) = \sqrt{\Omega_m(1+z)^3 + \Omega_\Lambda}$. At the redshift of A2319, 1 arcmin corresponds to approximately 64.9 kpc. Uncertainties are provided at the 1σ confidence level.

In the following, we refer to, and plot as reference, some characteristic radii, $R_{500} = 1368$ kpc and $R_{200} = 2077$ kpc, that are defined at the overdensities of $\Delta = 500$ and 200, respectively, with respect to the critical value $\rho_c = 3H_0^2 \frac{E(z)^2}{8\pi G}$ and using the hydrostatic mass profile (see Table 4 in Section 4.4).

2. XMM-Newton Analysis

X-ray spatial and spectral analysis provide a direct probe of density and temperature of the ICM. However, the X-ray background needs to be modelled very accurately if we want to obtain accurate measurements in the outskirts of galaxy clusters, where the background dominates over the signal.

2.1. Data reduction

The *XMM-Newton* Science Analysis System (XMM-SAS v15.0) and the corresponding calibration files have been used to reduce the X-ray data, following the Extended Source Analysis Software analysis scheme (ESAS; Snowden et al. 2008). The presence of anomalous individual CCDs is also taken into account, removing them from the analysis. Soft proton flares periods are filtered out using the ESAS tasks *mos-filter* and *pn-filter*, therefore obtaining clean events files. The ESAS procedure *cheese* is adopted in order to mask point sources which contaminates the field of view.

Spectra, effective areas and response files (ARF and RMF respectively) for the selected regions are extracted using the ESAS tasks *mos-spectra* and *pn-spectra*.

This procedure is applied to all the seven observations we use in the analysis of Abell 2319: an archival central exposure, four offset observations (done specifically for the X-COP program), and two other archival exposures pointing just outside the virial radius, which are used to estimate the local sky background. Table 1 provides some information regarding these observations, like the OBSID, the total and the clean exposure time, and the level of soft protons contamination, obtained comparing the measured count rate in a hard spectral band in the exposed and unexposed part of the field of view (inFOV/outFOV, Leccardi & Molendi 2008).

2.2. Particle background modeling

We extracted count images from the cleaned event files in the [0.7 - 1.2] keV energy band, where we expect to maximize the signal-to-background ratio (e.g. Etori et al. 2010; Etori & Molendi 2011). In Appendix A we present our method to model the 2D distribution and intensity of the non X-ray background (NXB), distinguishing its different components, and computing the total NXB image in the required energy band. We briefly summarize the main steps here.

The *XMM-Newton* NXB is made of three separate components: the quiescent cosmic-ray induced particle background (QPB), the soft protons (SP), and a stable quiescent component (QC), whose origin is yet unknown (Salvetti et al. 2017). To model the QPB, we used the unexposed corners of the EPIC cameras to estimate the QPB level in each observation. We then use filter-wheel-closed observations to model the spatial distribution of the QPB and renormalize the filter-wheel-closed data to match the count rate measured in the unexposed corners.

The residual contribution after subtraction of the QPB is split between the QC and SP components. In Appendix A we describe our method to take the relative contribution of these two components into account. Briefly, we measure radial surface brightness profiles for a large sample of 495 blank-sky pointings and we optimize the relative contribution of these components as a function of the estimated SP contamination, imposing that the residual surface brightness profiles be consistent with a flat curve in the energy band of interest. This procedure leads to an accurate modeling of the SP contamination, as shown in Fig. A.1. The deviations from a flat profile are found to be at the level of less than 5%, thus for the remainder of the paper we adopt a systematic uncertainty of 5% of the NXB level on the measured surface brightness profile.

Observation	OBSID	Total [ks]	MOS1 [ks]	MOS2 [ks]	<i>pn</i> [ks]	inFOV/outFOV
Center	0600040101	58.3	48.3	49.3	41.1	1.215
North	0744410101	36.0	23.8	24.5	19.4	1.132
South	0744410301	31.0	13.8	14.0	7.0	1.406
East	0744410401	41.9	14.4	15.4	9.5	1.346
West	0744410201	37.5	23.4	25.1	9.8	1.152
Outside	0743840201	15.0	12.1	12.3	5.7	1.261
Outside2	0763490301	18.0	12.9	12.8	9.0	1.253

Table 1. Pointing name, OBSID, total exposure time and clean exposure time for MOS1, MOS2, and *pn*, and inFOV/outFOV ratio, for the seven observations used in this work. All the observations are obtained using the medium filter, the full frame science mode for MOS and extended full frame for *pn*.

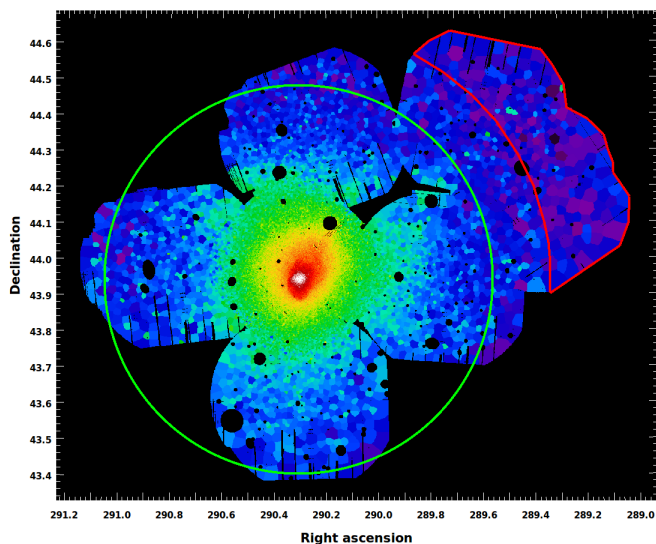


Fig. 1. Mosaicked and Voronoi tessellated image of A2319, in the energy band [0.7-1.2] keV, corrected for the particle background. The red region is the one chosen for the estimate of the local sky background. The green circle represents the location of R_{200} .

2.3. Spatial analysis

We combine the results from MOS1, MOS2 and *pn* and mosaicked all seven observations into one single image.

We filter our image one more time by using the *Chandra* tool *wavdetect*, in order to find the remaining point sources which contaminates the field of view but were missed by the ESAS task *cheese*. Indeed this procedure has some difficulties finding some obvious point sources, lying near the gaps of the CCDs, or not found due to the parameters adopted.

A Voronoi tessellation algorithm (Diehl & Statler 2006) was applied on the mosaicked count image to create an adaptively binned surface-brightness map with a minimum of 20 counts per bin. The resulting Voronoi tessellated count rate map for A2319 is shown in Fig. 1.

In order to analyze spatially the cluster's image, we choose a background region located as far as possible from the cluster's center in order to have a good estimate of the sky background, minimizing the cluster contamination. We choose all the pixels in the image beyond 42 arcmin from the cluster's center to be the region where we estimate the local sky background (the red region in Fig. 1). The background level is just the mean count rate in this region: $(1.82 \pm 0.06) \times 10^{-4}$ cts s^{-1} arcmin $^{-2}$, in the energy band [0.7-1.2] keV (or, converting in flux using

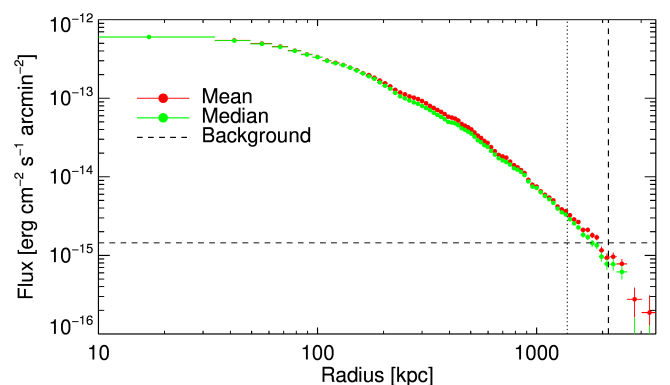


Fig. 2. Background subtracted surface brightness profiles in the [0.7-1.2] keV energy band, using the mean and median methods, red and green points respectively. The sky background level is shown with a horizontal dashed line. The vertical dotted and dashed lines represents the location of R_{500} and R_{200} , respectively.

a power law spectral model with photon index 1.41: $1.46 \pm 0.05 \times 10^{-15}$ erg s^{-1} cm^{-2} arcmin $^{-2}$).

The background-subtracted surface brightness profile is then computed in annular regions. We choose the annuli such that the total amount of net count rate in the [0.7-1.2] keV energy band is the same in all the regions. This choice ensures comparable statistics in all annuli. Using the ARF and RMF files for MOS2 (since the combined image was in units of MOS2), we are able to convert from count rates to fluxes. As shown in Fig. 2, we have also evaluated the surface brightness from both the azimuthal mean and the azimuthal median of the brightness distribution. Following the analysis in hydrodynamical simulations on the effects of the densest substructures on the average gas density profile (Zhuravleva et al. 2013; Roncarelli et al. 2013), Eckert et al. (2016) showed that the median is indeed less biased than the mean, since it is a more robust estimator since it is unaffected by compact X-ray substructures filling a small fraction of the total volume, and that the ratio between mean and median can be used to estimate the relative impact of the detected clumps, providing an estimate of the level of gas clumpiness.

The electron density is then recovered using two different techniques: the onion-peeling technique (e.g. Ettori et al. 2010), and the multiscale technique (Eckert et al. 2016). Both assume the emission to be spherically symmetric. The latter technique requires also a super-parametric functional form for the density profile, decomposing the surface brightness in a very large number of β -models which can be individually deprojected. We obtain electron density profiles that are consistent within 0.7σ , and mean relative deviation of 5% up to the virial radius (see Fig. 3).

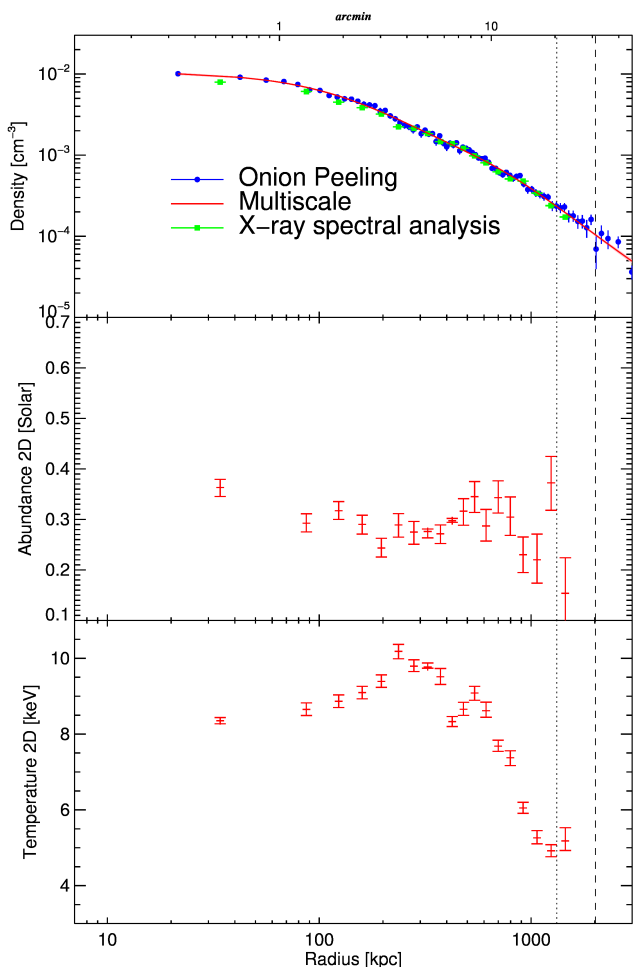


Fig. 3. (Top) Density profile recovered from the median surface brightness profile, using the multiscale and the onion peeling technique, red line and blue points respectively. The density coming from the spectral analysis is also shown here, green points. Abundance (Middle) and temperature (Bottom) from the fitting of the spectra in 19 annular regions. The vertical dotted and dashed line indicates the location of R_{500} and R_{200} respectively.

2.4. Spectral Analysis

In order to recover the electron temperature and metal abundance of the X-ray emitting plasma, we perform a spectral analysis by fitting the spectra with an absorbed thermal component in the energy range [0.5-11.3] keV, and excluding the spectral regions with strong instrumental emission lines ([1.2-2.0] keV for MOS and [7.1-9.2] keV for *pn*), using XSPEC (Arnaud 1996).

We extract spectra in 19 concentric annuli, defined in order to reach an approximately constant count rate in the [0.7-1.2] keV energy band. The number of net counts in the [0.5-11.3] keV energy band and the signal to background ratio are listed in Table B.1. We extract spectra also from the background region indicated in Fig. 1, which is the same region used to estimate the local sky background for the spatial analysis and where there is no evidence for cluster emission.

To model spectrally the NXB component, we follow Leccardi & Molendi (2008), modeling the spectra from the unexposed region of the instruments, the QPB component, using a broken power law in the energy range [0.5 - 11.3] keV for MOS and

in [0.5 - 14.0] keV, excluding the energy bands [7.1 - 9.2] keV where we observe strong instrumental emission lines for *pn*. We fit the background spectra, produced by the ESAS tasks *mos-back* and *pn-back*, which yields the unexposed spectrum representative of the QPB component. This fixes the parameters of the QPB background component.

Then, in the source spectrum, we restrict to a hard band, above 5 keV, and we model the remaining particle background component using a broken power law with shape parameters (i.e. slopes and break energy) fixed accordingly to the results obtained in other works (see Kuntz & Snowden 2008; Leccardi & Molendi 2008), leaving only normalization free. We include in the fit a thermal component (*apec* model in the X-ray spectral fitting package XSPEC, version 12.9.1; see Arnaud 1996), with only normalization free, and using a temperature of 9.6 keV (Molendi et al. 1999), redshift of 0.0557 (Struble & Rood 1999) and 0.3 solar abundance) considering that in the hard band the emission from the cluster is small but not negligible. In this way we fix the parameters describing the quiescent component.

We rescale the model particle background NXB, from the whole field of view to the local sky background region, leaving all the parameters of the models fixed. Normalizations are rescaled according to areas, i.e. if a spectrum comes from half of the field of view, normalizations are halved accordingly. This way the instrumental background and the contamination from soft protons are modelled in the background region. Then, we model the local sky background, that is the remaining source of emission in the background region. We construct the model using three different components:

- the Cosmic X-ray Background (CXB), that is modelled as an absorbed power law with photon index fixed to 1.41 (De Luca & Molendi 2004);
- the local bubble component, that is modelled as an unabsorbed thermal model with temperature free to vary around 0.11 keV (Liu et al. 2017), redshift equal to 0 and fixed solar elemental abundance;
- the galactic halo component, that is modelled as an absorbed thermal component with temperature free to vary around 0.22 keV (McCammon et al. 2002), redshift fixed to 0, and fixed solar elemental abundance.

Using the emission model $tbabs(apec+powerlaw)+apec$, we fit together all the spectra extracted from the background region and obtain the sky components with normalizations and temperatures listed in Table 2, which provide a flux of 1.7×10^{-15} erg/s/cm²/arcmin² in the energy band [0.7–1.2] keV.

Component	Normalization	Temperature
Galactic halo	1.0×10^{-4} cm ⁻⁵	0.35 keV
Local bubble	4.1×10^{-4} cm ⁻⁵	0.15 keV
CXB	1.1×10^{-4} $\frac{\text{photons}}{\text{keVcm}^2\text{s}}$ at 1 keV	/

Table 2. Components and parameters of the X-ray background adopted in our spectral analysis.

Similarly to the background region, we extract the spectra in the selected regions, and we rescale the particle background model for the NXB, from the field of view where they were calculated to the specific region of interest with just a change in normalization proportional to the areas. We obtain the sky background components from the background regions, rescaled according to the covered areas.

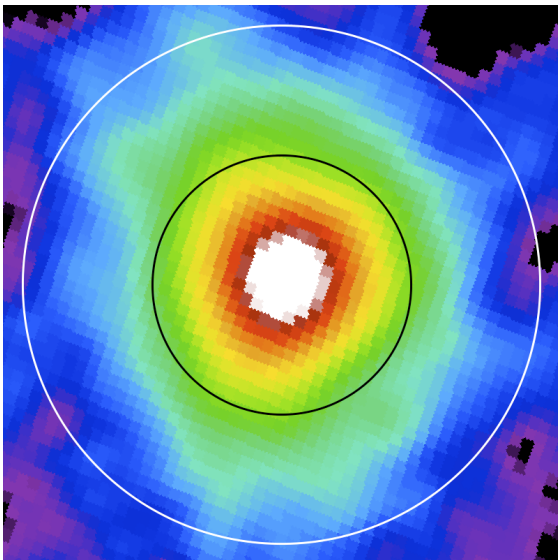


Fig. 4. Comptonization map of Abell 2319 reconstructed using MILCA (Hurier et al. 2013), with an angular resolution of 7 arcmin FWHM. The black and white circles indicates the location of R_{500} and R_{200} respectively.

We fix the particle and sky background. The cluster emission is modelled with a thermal component absorbed from our own Galaxy (model *tbabs* · *apec* in XSPEC). The gas temperature, abundance, and normalization are free parameters in the spectral fit, whereas the redshift is fixed. The galactic hydrogen column density is left free to vary between $7.2 \times 10^{20} \text{ cm}^{-2}$ and $12.8 \times 10^{20} \text{ cm}^{-2}$, where the lower value represents the minimum of the Galactic column density due to atomic hydrogen (as tabulated in LAB HI Galactic survey in Kalberla et al. 2005) estimated over the surveyed area, and the higher value indicates the maximum column density over the same area, also corrected for molecular hydrogen as suggested in Willingale et al. (2013).

We fitted jointly all the spectra belonging to the same annulus but extracted from different observations using the C-statistics. The best-fit parameters are shown in Fig 3 (with goodness of the fit, net counts, signal to background ratio, and best fit n_{H} indicated in Table B.1).

Modelling the ICM emission with a thermal component allows X-ray observations to provide a direct probe of the gas electron density, n_e . In fact its normalization K_{apec} can be written as:

$$K_{\text{apec}} = \frac{10^{-14} \text{ cm}^{-5}}{4\pi D_A(1+z)^2} \int_V n_e n_p dV \quad (1)$$

with the proton number density, n_p , is proportional to n_e ($n_p \sim 0.8n_e$).

We recover the 3D profiles, temperature and abundance, by adopting the ‘‘onion peeling’’ technique (Kriss et al. 1983; Ettori et al. 2002, and references therein). Assuming a constant gas density inside each shell, we can rewrite Eq. 1 as matrix product (using ‘‘#’’ to indicate it): $K_{\text{apec}} \propto V \# n_e^2$, where V_i^j is the geometrical volume of the j^{th} shell intercepted by the i^{th} annulus. By inverting this linear equation, we obtain the electron density inside each shell as $n_e \propto \sqrt{V^{T-1} \# K_{\text{apec}}}$. Values of the temperature and metal abundance in each shell are then obtained as $Y_{3D} = \frac{V^{Y-1} \# (Y_{2D} \cdot EM)}{V^{Y-1} \# EM}$, where $EM = \int n_e^2 dV$ is the emission measure and Y is the quantity of interest (either tempera-

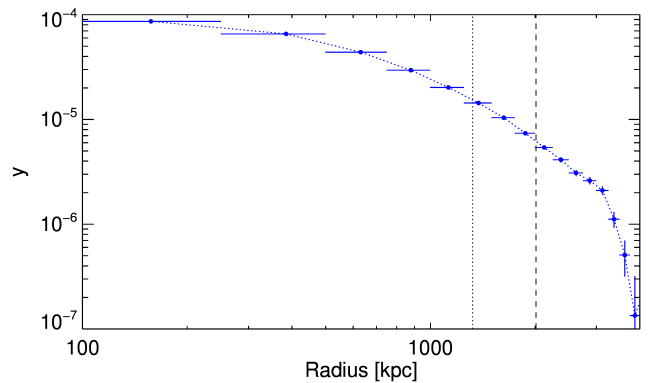


Fig. 5. Comptonization profile extracted from the SZ map. The vertical dotted and dashed line indicates the location of R_{500} and $2R_{500}$ respectively.

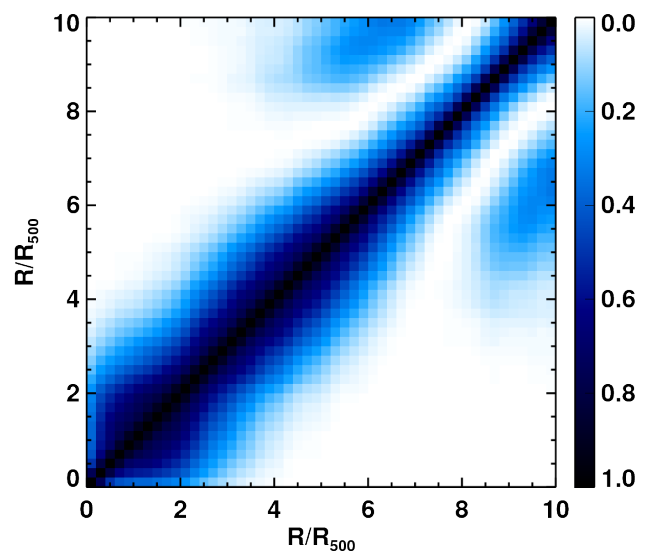


Fig. 6. *Planck* correlation matrix $\rho_{X,Y}$ for the unbinned Comptonization parameter profile.

ture or metallicity; for a discussion on the systematic effects see Ameglio et al. 2007) The errors are estimated through a Monte Carlo process.

3. Planck Analysis

The SZ effect provides a direct measurement of the thermal pressure integrated along the line of sight (Sunyaev & Zeldovich 1972). The dimensionless Comptonization parameter is defined as follow:

$$y(r) = \frac{\sigma_T}{m_e c^2} \int P_e(\ell) d\ell \quad (2)$$

where the integral is computed along the line of sight, ℓ , at the radius r from the centre. σ_T the Thomson cross section, m_e the mass of the electron, and c the speed of light.

The pressure profile is recovered from the SZ signal measured in the all-sky survey by the *Planck* mission (Tauber et al. 2010; Planck Collaboration et al. 2016a). The SZ signal map

is derived from the internal linear combination of the six frequency bands of the high frequency instrument (HFI; Lamarre et al. 2010; Planck HFI Core Team et al. 2011) on board the *Planck* satellite. More specifically, we made use of the Modified Internal Linear Combination Algorithm (MILCA, Hurier et al. 2013) which offers the possibility to reconstruct the targeted signal component at various scales contributed differently by the six combined input frequency maps. We therefore reconstruct a y -map for A2319 with an angular resolution of 7 arcmin FWHM (see Fig. 4).

From the y -map, we proceed according to the method used and detailed in Planck Collaboration et al. (2013).

We extracted the y -parameter radial profile of A2319 from our MILCA y -map. i.e., the profile is extracted on a regular grid with bins of width $\Delta\theta/\theta_{500} = 0.2$. The local background offset is estimated from the area surrounding the cluster beyond $5 \times \theta_{500} = 106$ arcmin. The resulting profile is shown in Fig. 5. The pressure profile is then obtained following the real space deconvolution and deprojection regularisation method first described in Croston et al. (2006), assuming spherical symmetry for the cluster. The correlated errors were propagated from the covariance matrix of the y profile with a Monte Carlo procedure and led to the estimation of the covariance matrix of the pressure profile $P_e(r)$.

Abell 2319 is the highest signal-to-noise ratio SZ detected cluster in the *Planck* SZ catalogues ($SNR \sim 50$; see Planck Collaboration et al. 2014, 2016b). Its proximity and its extension makes it fully resolved even at the moderate angular resolution of the *Planck* survey, and its SZ signal extends well beyond R_{500} with at high significance. We thereby were able to perform an azimuthal analysis in 8 azimuthally-resolved sectors (see Section 6). The y and pressure profiles in each sector were obtained as afore-described after masking the y -map and its associated error map according to the sector definition.

Due to the moderate angular resolution of the *Planck* survey and the oversampling implied by our sampling of the y -map, we introduced co-variance between the individual pixels. It cascades on the y and pressure profiles computation, hence their respective covariance matrix.

In Fig. 6 we show the correlation matrix between data points, defined as:

$$\rho_{X,Y} = \frac{\Sigma(X,Y)}{\sigma_X^2 \sigma_Y^2}$$

where Σ indicates the covariance matrix.

Consequently, we stress that points of our y and SZ pressure profiles are correlated and that the respective error bars displayed in the figures of this paper represent only the square root of the diagonal of the covariance matrix. Nevertheless when pressure is used to derive other quantities we make complete use of the whole covariance matrix, and therefore we consider any impact of the *Planck* PSF in our calculations.

4. Joint X-ray/SZ analysis of the thermodynamic properties

The profiles of the electron density estimated from X-ray and of the pressure obtained through SZ can be combined to recover all the thermodynamic quantities that define the properties of the ICM:

- the gas temperature:

$$T = P \cdot n_e^{-1} \quad (3)$$

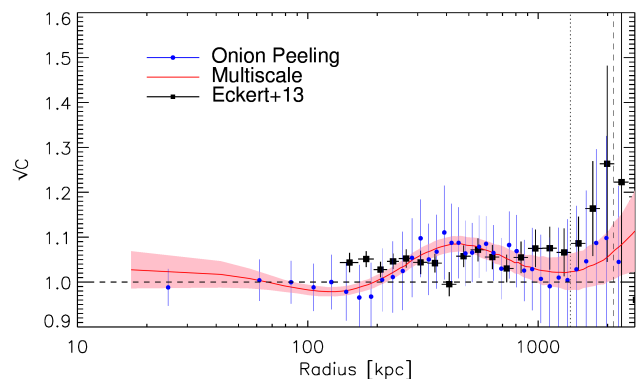


Fig. 7. Clumping factor radial profile for both the onion peeling (in blue) and the multiscale (in red) techniques. The pink area represents the 1- σ confidence interval around the multiscale clumping factor. The black squares represents the observed value for the clumpiness in the work of Eckert et al. (2015). The vertical lines mark the position of R_{500} and R_{200} , dotted and dashed respectively.

- the gas entropy:

$$K = T \cdot n_e^{-2/3} = P \cdot n_e^{-5/3} \quad (4)$$

- the gas mass:

$$M_{\text{gas}}(< R) = 4\pi \int_0^R \rho_g(r') r'^2 dr' \quad (5)$$

where the gas mass density $\rho_g = (n_e + n_p)m_u\mu$ with m_u being the atomic mass unit and $\mu \approx 0.6$ the mean molecular weight in a.m.u.;

- the hydrostatic gravitating mass:

$$M_{\text{tot}}(< r) = -\frac{r^2}{G\rho_g(r)} \frac{dP_g(r)}{dr} \quad (6)$$

where G is the gravitational constant, and the gas pressure P_g satisfies the ideal gas law $\rho_g kT / (\mu m_u) = P_g$. The gas mass fraction is then defined as $f_{\text{gas}} = M_{\text{gas}} / M_{\text{tot}}$.

4.1. Clumpiness profile

X-rays imaging can be directly used to estimate the level of inhomogeneities present in the ICM. The clumping factor $C = \langle n_e^2 \rangle / \langle n_e \rangle^2$ measures the bias that affects the reconstruction of the gas density from the X-ray emission, that is directly proportional to n_e^2 . Since we are considering the X-ray signal collected in a narrow energy range, [0.7–1.2] keV, that is almost insensitive to the gas temperature, we can directly use the results from the spatial analysis to estimate the gas clumping factor C .

In first approximation, the density distribution inside a volume shell can be described by a log-normal distribution skewed by the presence of denser outliers, clumps (Zhuravleva et al. 2013; Roncarelli et al. 2013). Therefore, while the mean of this distribution tends to overestimate the gas density, the median is robust against the presence of clumps (Eckert et al. 2015), and we can estimate C as the ratio of the deprojected X-ray surface brightness profiles obtained from (i) the mean of the azimuthal distribution of the counts in annuli and (ii) the median of the same distribution. The resulting profile is shown in Fig. 7 and indicates a \sqrt{C} of about 1.1 at R_{200} .

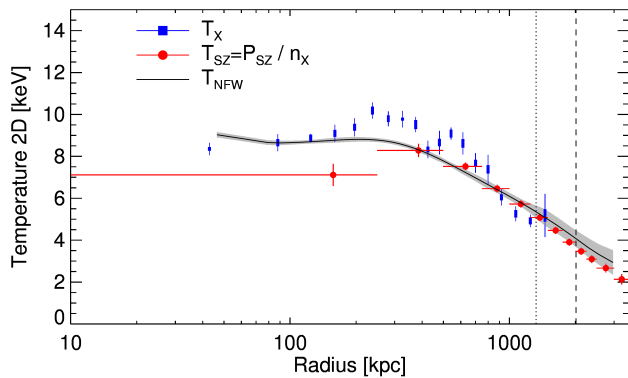


Fig. 8. Two-dimensional temperature profiles using X-ray spectral data (blue points; thick errorbars represent the systematic uncertainty as estimated in Section 4.2.1; thin errorbars indicate the total uncertainties), the pressure from SZ divided by density from X-ray projected on the plane of the sky (red points) and the projection of the reconstructed temperature from the *backward* technique, which makes use of both X-ray and SZ data, on an NFW mass model (black line). The grey shaded area is the 1σ confidence region around the *backward* result. The vertical lines mark the position R_{500} and R_{200} , dotted and dashed respectively.

However we can only detect clumps that are resolved by *XMM-Newton*, i.e. clumps on scales larger than the PSF half energy width (~ 17 arcsec ≈ 18.4 kpc, for MOS¹; see also Read et al. (2011)). This implies that clumped structures below this scale might still bias our measured thermodynamic quantities.

4.2. Temperature profile

Similarly to what has been done for the pressure, we can recover the ICM temperature profiles in two different ways: (i) from the spectral analysis (T_X) as detailed in Sect.2.4; (ii) by dividing P_{SZ} with the gas density n_e recovered from the deprojection of the X-ray surface brightness (T_{SZ}). These values can be compared with the profile T_{NFW} that is obtained from the best-fit mass model (see Section 4.4) by requiring that the hydrostatic equilibrium holds between the cluster potential and the observed gas density profile. Note that T_{NFW} is not independent from the other two profiles, because the best-fit mass model is obtained by fitting both the measured T_X and P_{SZ} . In order to obtain a meaningful comparison with T_X , we compute an spectroscopic-like projection (see Mazzotta et al. 2004; Morandi et al. 2007) of the three-dimensional quantities T_{SZ} and T_{NFW} . The good agreement among these profiles is shown in Fig. 8.

We notice that, since the pressure gradient in the first point is washed out from the *Planck*'s beam of about 7 arcmin, the pressure in this point is underestimated, and therefore also the temperature T_{SZ} is underestimated with respect to T_X .

4.2.1. Systematic uncertainties on the temperature profile

We constrain the projected spectroscopic temperature (see Sect.2.4) with a relative statistical uncertainty ranging between 1 and 6 per cent (median value: 2%). It is thus critical to evaluate the role of possible systematics in our measurements. In order to calculate some of the most relevant systematic uncertainties affecting our temperature measurements, we re-estimate the spectral temperature using several different methods. Our reference temperature measurement is the one calculated using both

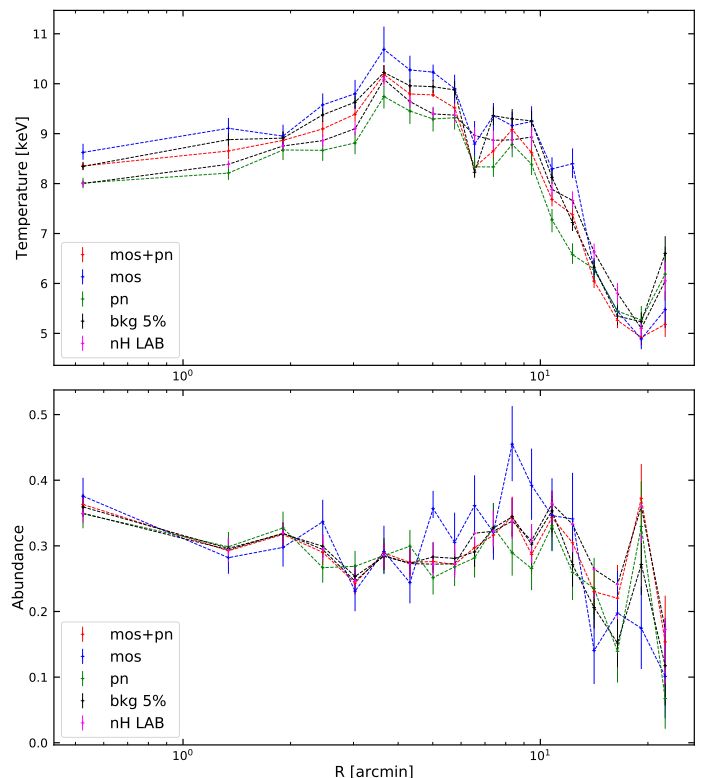


Fig. 9. Temperature and abundance profile adopting different techniques, this allows to have an estimate of the systematic error affecting our measurement.

MOS and *pn* data, leaving n_H free to vary within a defined narrow range, and fixing the parameters of the background model. By changing all these quantities, one by one, we estimate the level of systematic errors that affect our measurements. In details, we calculate the spectral temperatures (i) using only counts collected from MOS (ii) only from *pn*, (iii) fixing n_H to the LAB value (Kalberla et al. 2005), and (iv) allowing the background parameters (normalizations) to vary within $\pm 5\%$ of the best-fit values. We show in Fig. 9 the results of this procedure. Finally, at each radial point, we estimate the systematic error using the standard deviation of the values measured with all the different methods. This error is then added, in quadrature, to the statistical error and propagated through the entire analysis. The relative systematic error ranges between 1.4% and 9.1%, apart from the outermost radial point where we measure a value of 19%.

4.3. Pressure profile

If the galaxy cluster is not affected by an ongoing merger generating shocks through the ICM, the pressure is the thermodynamic quantity that presents a smoother spatial distribution along the azimuth. It is well described by an “universal” form (Nagai et al. 2007; Arnaud et al. 2010):

$$\frac{P(x)}{P_{500}} = \frac{P_0}{(c_{500}x)^\gamma [1 + (c_{500}x)^\alpha]^{\frac{\beta-\gamma}{\alpha}}}, \quad (7)$$

where

$$P_{500} = 1.65 \times 10^{-3} \text{ keV cm}^{-3} \left(\frac{M_{500}}{3 \times 10^{14} M_\odot} \right)^{2/3} E(z)^{8/3} \quad (8)$$

¹ <https://heasarc.nasa.gov/docs/xmm/uhb/onaxisxraypsf.html>

	P_0	c_{500}	γ	α	β	χ^2	d.o.f.
Arnaud et al. (2010)	8.40	1.18	0.31	1.05	5.49	-	-
Planck Collaboration et al. (2013)	6.41	1.81	0.31	1.33	4.13	-	-
SZ+X	7.7 ± 2.0	1.34 ± 0.22	0.47 ± 0.07	1.05	3.80 ± 0.22	2.62	69
SZ	9.6 ± 5.8	1.10 ± 0.35	0.23 ± 0.23	1.05	4.50 ± 0.47	3.47	9

Table 3. Best fit parameters of the pressure profile using the functional form introduced by Nagai et al. (2007). “SZ+X” refers to the best fit done on the best fit mass model pressure profile(see Sec. 4.4), while “SZ” refers to the best fit done only on the P_{SZ} .

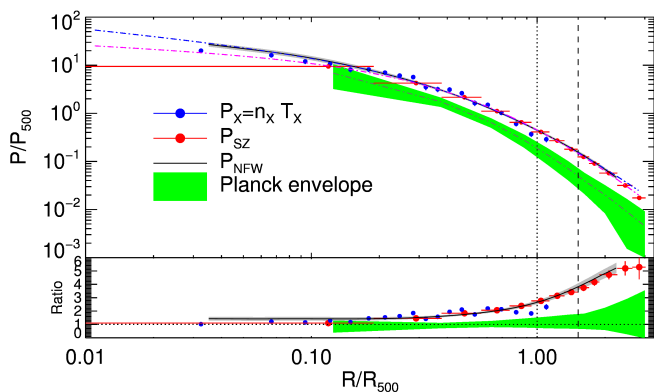


Fig. 10. Rescaled pressure profile in units of R_{500} . The grey dashed line represents the “universal” pressure profile. The blue and the pink lines represents the best fits using the functional form introduced by Nagai et al. (2007) done on, P_{NFW} and P_{SZ} , respectively. The dotted and the dashed vertical lines represent the position of R_{500} and R_{200} respectively. In the bottom panel we show the ratio of P_{SZ} , P_X , and P_{NFW} with the “universal” pressure profile(Arnaud et al. 2010).

and $x = R/R_{500}$; γ , α , and β are the central slope, the intermediate slope, and the outer slope defined by a scale parameter $r_s = R_{500}/c_{500}$ ($R \ll r_s$, $R \sim r_s$ and $R \gg r_s$ respectively), and P_0 is the normalization. The values of R_{500} and M_{500} adopted here are presented in Table 4 (see Section 4.4). We list in Table 3 our best-fit values, using all the available radial range to fit.

The electronic pressure can be directly recovered both from the comptonization profile (see Eq. 2; P_{SZ}), and from deprojection of X-rays measurements of the temperature and density profiles of the emitting electrons (P_X). We can also estimate the pressure profile required from the best-fit mass model to satisfy the hydrostatic equilibrium (P_{NFW} , see Section 4.4). As we show in Fig. 10, these 3D pressure profiles agree well within their statistical errors.

We rescale the pressure profile by P_{500} and fit it with the “universal” functional form (Nagai et al. 2007). The best fitting results are tabulated in Table 3. The comparison with the results of *Planck* (Planck Collaboration et al. 2013) and Arnaud et al. (2010) is shown in Fig. 10. We observe that the pressure profile in A2319 is well above the other two profiles, in particular in the outskirts, with values higher by about a factor ~ 3.5 at R_{200} , which is $\sim 2\sigma$ away from the *Planck* envelope (Planck Collaboration et al. 2013).

We have also adopted a new technique (Bourdin et al. 2017) in order to evaluate the impact of the anisotropies in the Compton parameter detected in the outskirts of A2319 on the reconstructed pressure profile, and conclude that these anisotropies cannot explain the observed excess.

4.4. Hydrostatic mass

The total mass profile of the cluster is reconstructed by solving the hydrostatic equilibrium equation 6 (HEE, Binney & Tremaine 1987). In this work, we use three different methods to solve this equation and recover the hydrostatic mass profile (e.g. Ettori et al. 2013): the *backward* method, the *forward* method and a *non-parametric* method.

The *backward* method follows the approach described in Ettori et al. (2010, 2017) and, assuming a mass model with few (in general, two) free parameters, minimizes a likelihood function by comparing the predicted and observed profiles of some interesting physical quantities (such as the temperature) to constrain these parameters. In the present analysis, we assume a Navarro-Frenk-White profile (NFW, Navarro et al. 1997) for the total mass (a more extensive discussion on the best-fitting mass models will be presented in a forthcoming publication), and constrain its two parameters, concentration and scale radius (or R_{200}), using both the projected temperature profile from X-ray spectral analysis and the thermal pressure profile from the SZ analysis, and maximizing the likelihood described in Appendix D.

In Fig. 11, we show the best fit results obtained using this method to constrain the parameters of the mass model, using the median method and the multiscale technique to obtain the density profile. Very consistent results are obtained by adopting different methods to recover the input profiles of the gas temperature and density (see Table 4). We indicate with the subscript “NFW” the thermodynamic quantities corresponding to the best-fit mass model.

In the *forward* method, functional forms are used to fit the thermodynamic quantities, like density, pressure and temperature. Then, HEE is directly applied in order to compute the total mass radial distribution. Errors are estimated through a Monte Carlo process. As mentioned in Section 2.3, we use the multiscale approach (Eckert et al. 2015) to fit the emissivity profile which yields directly the fitted density functional form. We use a 6-parameters functional form (Vikhlinin et al. 2006) to fit the temperature, and a 5-parameters generalized NFW (Nagai et al. 2007) for the pressure. We combine in several ways the profiles of the thermodynamic quantities (density, pressure and temperature), as detailed in Table 4, making use of a joint likelihood (see Appendix D) when all 3 quantities are fitted together. It is worth noticing that, while measurements of the gas density and pressure are available up to $\sim R_{200}$, direct spectral estimates of the temperature are limited to regions below R_{500} , defining the radial range where the mass profile is more reliable in this case.

Due to the good quality data both from X-rays and SZ, we can also implement a *non-parametric* method in order to recover the total mass profile. We just insert pressure and density in the HEE, and we calculate the pressure derivative using a three-point quadratic Lagrangian interpolation. We point out that the errors relative to this method are represented by a covariance matrix, since we are using the SZ pressure profile, and therefore what

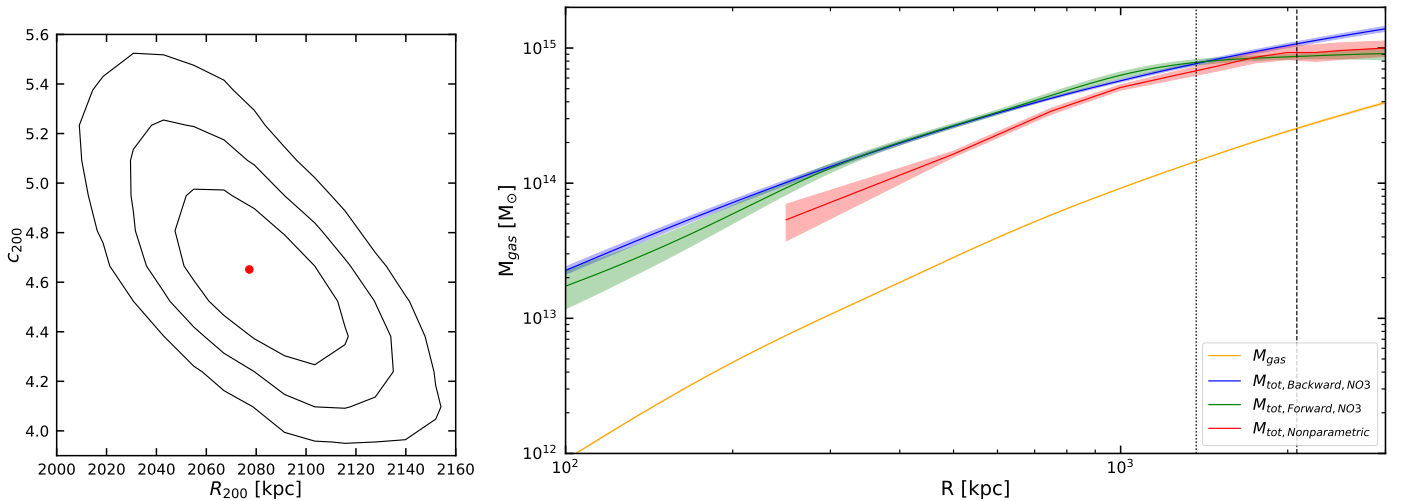


Fig. 11. (Left) Contour plot with confidence regions at 1, 2, 3 σ (solid lines) applying the *backward* approach to solve HEE in order to constrain the parameters of the NFW mass model; using as inputs the multiscale technique on the median emissivity profile to obtain the density, the pressure from the direct deprojection of the y -parameter radial profile, and the temperature from the spectral analysis. (Right) Gas mass and total mass profile recovered using *backward* approach (blue and red curves, respectively). The black crosses represent the total mass profile obtained using a non-parametric method and the green one by applying the *forward* method on temperature and density profiles. The vertical lines mark the positions of R_{500} and R_{200} , dotted and dashed respectively.

Technique	Data	M_{200} ($10^{14} M_{\odot}$)	R_{200} (kpc)	M_{500} ($10^{14} M_{\odot}$)	R_{500} (kpc)
<i>backward</i>	$P_{SZ,NO3} + T_X$ - Median	10.7 ± 0.5	2077 ± 33	7.7 ± 0.4	1368 ± 17
<i>backward</i>	$P_{SZ} + T_X$ - Median	10.6 ± 0.5	2071 ± 32	7.5 ± 0.3	1357 ± 13
<i>backward</i>	$P_{SZ,NO3} + T_{X,SYS}$ - Median	10.3 ± 0.7	2047 ± 47	7.4 ± 0.4	1350 ± 24
<i>backward</i>	$P_{SZ} + T_{X,SYS}$ - Median	10.5 ± 0.5	2062 ± 34	7.3 ± 0.3	1347 ± 18
<i>forward</i>	P_{SZ} only - Median	9.4 ± 0.5	1984 ± 40	7.4 ± 0.4	1353 ± 25
<i>forward</i>	T_X only - Median	/	/	7.3 ± 0.1	1343 ± 5
<i>forward</i>	$P_{SZ} + T_X$ - Median	8.3 ± 0.3	1906 ± 20	7.8 ± 0.2	1375 ± 11
<i>forward</i>	$P_{SZ} + T_X, \beta$ fixed - Median	8.5 ± 0.6	1923 ± 48	7.7 ± 0.4	1368 ± 26
<i>forward</i>	$P_{SZ,NO3} + T_{X,SYS}, \beta$ fixed - Median	7.7 ± 0.7	1859 ± 59	7.4 ± 0.6	1354 ± 37
<i>forward</i>	$P_{SZ,NO3,SYS} + T_X$ - Median	8.3 ± 0.3	1907 ± 26	7.8 ± 0.3	1373 ± 18
<i>non parametric</i>	P_{SZ} - Median	9.3 ± 1.1	1979 ± 78	6.7 ± 0.5	1307 ± 33
<i>backward</i>	$P_{SZ} + T_X$ - Mean	10.2 ± 0.5	2040 ± 35	7.3 ± 0.3	1346 ± 17

Table 4. Best fitting results on the mass model using different techniques, as specified in the first column. In the second column, the data used to constrain the mass are listed; P_{SZ} and T_X refers to the SZ pressure and the X-ray temperature respectively; the subscript “NO3” indicates that the first 3 *Planck* points were not used in the analysis; the subscript “SYS” indicates that the systematic uncertainties on the X-ray temperature are added in quadrature to the statistical errors in evaluating the χ^2 (see Sec. 4.2.1); “Median” or “mean” refers to how we computed the X-ray emissivity; “ β fixed” indicates that the outer slope of the pressure profile is fixed to the best fit value of the *Planck* collaboration. In the other four columns, we quote the results on M_{200} , R_{200} , M_{500} , and R_{500} respectively. In the first row, we indicate our reference values in the bold font. The last two rows present the mass reconstructed using the mean density profile, and propagating the statistical error on the temperature profile only (See Section 4.2.1). R_{Δ} are defined as $\left(\frac{M(R)}{4/3\pi\rho_c\Delta}\right)^{1/3}$.

is shown as an errorbar in the plot is just the square root of the diagonal terms.

The recovered mass profiles are shown in Fig. 11. They are all compatible within their respective error bars at the characteristic overdensities of 500 and 200.

4.4.1. Systematic uncertainties on the hydrostatic mass

In Table 4, only the statistical error on M_{200} (with a relative uncertainty of about 4.7%) is quoted. In this section, we evaluate what is the impact of some of the systematic uncertainties that affect the mass reconstruction.

The ability of the particle background model to reproduce a flat surface brightness profile when applied on blank field observations is a source of systematic uncertainty caused by the adopted procedure. As we discussed in Section 2, adopting the background modeling described in Appendix A, we are able to reduce the systematic deviation from a flat profile below 5%. We account for this by adding 5% of the background level as an extra error in the surface brightness profile.

The results obtained applying different methods and techniques are shown in Table 4. We estimate the level of the systematic uncertainties on the mass measurement at R_{500} and R_{200} of about 3.9% and 8.4%, respectively, by measuring the relative scatter around the reference value.

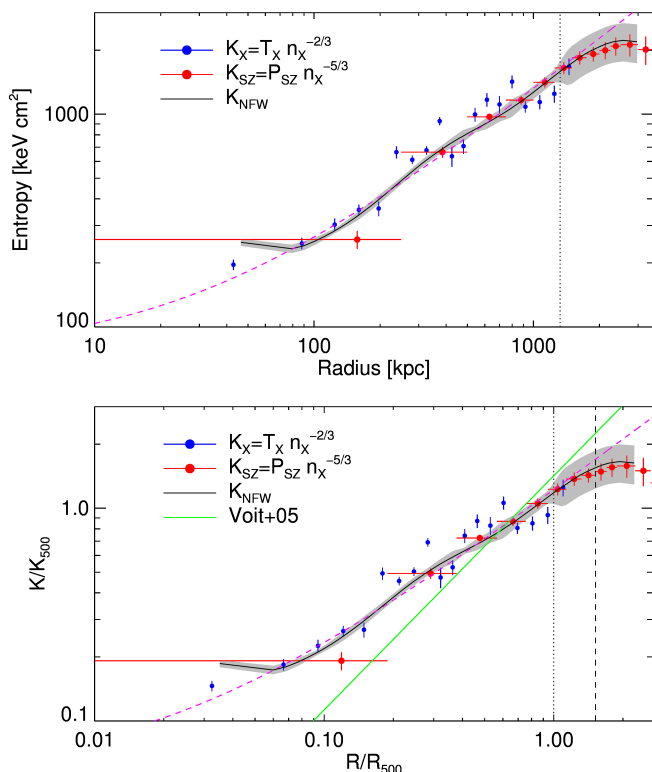


Fig. 12. (Top) Entropy profiles obtained from the three different methods described in Sec. 4.5. The dashed magenta line represents the best fit obtained on the K_{NFW} data using Eq. (9). (Bottom) Entropy profiles rescaled by K_{500} . The dashed magenta line represents the best fit obtained on the K_{NFW} data using Eq. (12). The green lines represents the prediction from Voit et al. (2005). The dashed pink lines are the best fit using Eq. (9) and (12). The vertical dotted and dashed lines represents the location of R_{500} and R_{200} , respectively.

Another source of systematic uncertainty comes from the choice of the background region, defined in an area concentrated to the West of the cluster. Considering that A2319 has an angular extension of ~ 1 degree, cosmic variance can influence the analysis, especially in the outskirts. Using the absorbed thermal model *tbabs(apec)*, and fixing the parameters of the *apec* component, we vary the hydrogen column density only, by adopting the values of n_H in regions located at North, West, East, and South, as far as possible from the center (distance of 33, 55, 36, and 39 *arcmin* respectively) and re-measure the conversion factor between the count rate and the surface brightness maps. This procedure allows to measure a relative deviation of 2% on the surface brightness, that translates into an effect of about 1.4% on the gas density and 1.1% on the mass measurement.

We therefore estimate that the total systematic uncertainties are at the level of 4.18% and 8.5% at R_{500} and R_{200} , respectively, implying that the reference values for the hydrostatic mass are, at R_{500} and R_{200} , respectively:

$$M_{500} = 7.7 \pm 0.4^{\text{stat.}} \pm 0.3^{\text{syst.}} \times 10^{14} M_{\odot}$$

$$M_{200} = 10.7 \pm 0.5^{\text{stat.}} \pm 0.9^{\text{syst.}} \times 10^{14} M_{\odot}$$

4.5. Entropy profile

The entropy profile is recovered through the gas pressure and temperature profiles via Eq. (4). Entropy is a fundamental quantity to track the thermal history of a cluster: it always rises when

a heat flow occurs, and in the presence of just non-radiative processes it is expected to follow a power law with characteristic slope of 1.1 (Tozzi & Norman 2001; Voit et al. 2005). Deviations from this power law are observed in the central regions, requiring an entropy “floor” within ~ 100 kpc that is expressed through the formula (Cavagnolo et al. 2009):

$$K = k_0 + k_{100} \left(\frac{R}{100 \text{ kpc}} \right)^{\alpha} \quad (9)$$

The central entropy (k_0) measured with the fit in Eq. (9) is $75 \pm 13 \text{ keV cm}^2$ (see Table 5), suggesting that A2319 does not possess a relaxed, cool core (e.g. Cavagnolo et al. 2009, define a CC when $k_0 < 50 \text{ keV cm}^2$).

However non-radiative simulations show that the self similar behaviour is reproduced only once entropy is rescaled by a proper quantity defined with respect to the critical density (Voit et al. 2005):

$$K_{500} = 106 \text{ keV cm}^2 \left(\frac{M_{500}}{10^{14} M_{\odot}} \right)^{2/3} E(z)^{-2/3} f_b^{-2/3} \quad (10)$$

where $f_b = 0.15$ is the universal baryon fraction. Non-radiative simulations (Voit et al. 2005) predicts that the power law describing the entropy profile is:

$$\frac{K(R)}{K_{500}} = 1.42 \left(\frac{R}{R_{500}} \right)^{1.1} \quad (11)$$

In order to accommodate the flattening of the entropy profile observed in many disturbed system we add a constant to a simple power law:

$$\frac{K(R)}{K_{500}} = k_0 + k_{500} \left(\frac{R}{R_{500}} \right)^{\alpha}, \quad (12)$$

In Fig. 12, we plot the measured entropy profiles, also rescaled accordingly to Eq. 12. In Table 5, we show the best fit results on the data using Eq.(9) and (12). We observe that the entropy profile has a shallower slope with respect to what is predicted by simulations (Voit et al. 2005).

5. Analysis in Azimuthal Sectors

Considering the high signal-to-noise ratio of our X-ray and SZ datasets, we can perform the analysis presented in the previous Sections in each of the 8 azimuthal sectors with width of 45° that we define in Fig. 13. The analysis performed in sectors allows us to measure the azimuthal variance of the physical quantities and to assess which are the cluster regions more relaxed. Indeed, by dividing the observed count rate map in Fig 1 with a cluster model with perfect spherical symmetry and emission equal to the azimuthal median surface brightness profile, we can identify where an excess in the emission due to the ongoing merger is located. As shown in Fig. 13, this excess is concentrated in the NW region (Sectors 1, 2 and 3, in particular).

We show the profiles of the thermodynamic properties recovered in 8 angular sectors in Fig. 14.

In the X-ray surface brightness, we identify various features specific in each sector:

- Sector 1 has an excess in emission starting above 200 kpc with a small radial extent of about 100 kpc. This excess is due to a contamination of the merging component in this cluster, located 10 *arcmin* NW.

	k_0	$k_{100/500}$	α	χ^2	d.o.f.
Eq. (9)	75 ± 13	190 ± 12	0.82 ± 0.03	129	70
Eq. (12)	0.055 ± 0.010	1.17 ± 0.02	0.82 ± 0.03	124	70

Table 5. Best fit results for the model of the entropy profile using the three different rescaling described in the Sec. 4.5.

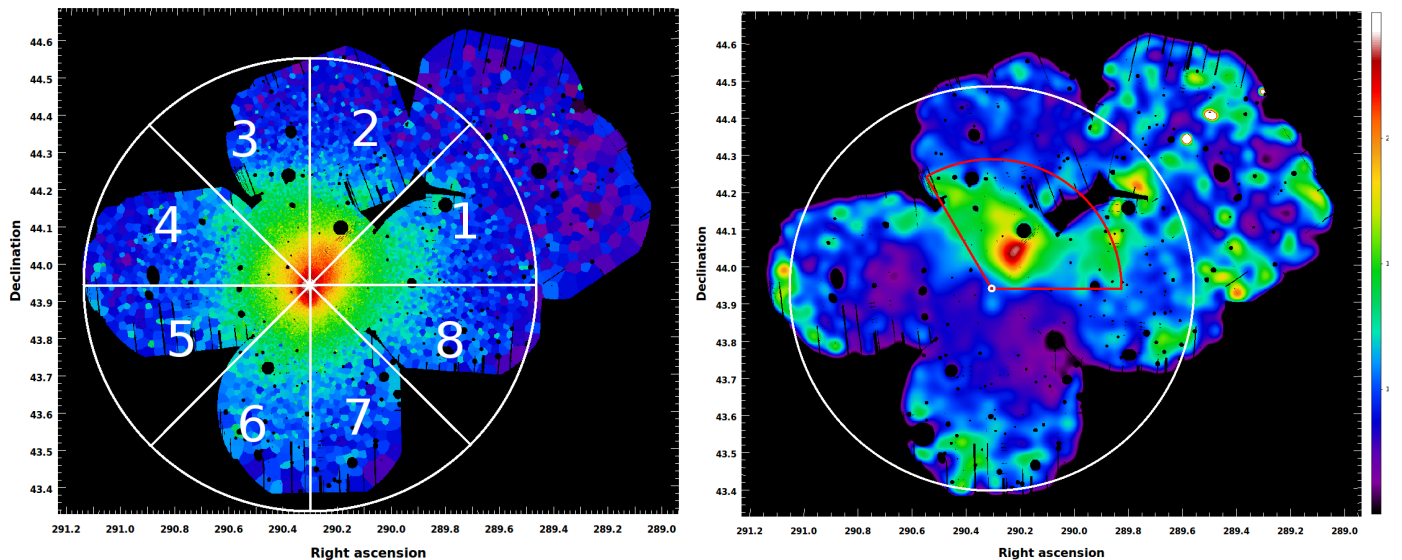


Fig. 13. (Left) Same as Fig. 1. The white sectors represents the 8 regions analyzed separately, each one is marked by a identification number. (Right) Residual image obtained by dividing the flux image by the model image reconstructed from the median method. The small white circle represent the center of the cluster, and the big white circle represents the position of R_{200} . The red sector represents the region which shows a clear excess in the residual map.

- Sector 2 has also a significant excess in the X-ray emission. This excess is located in the region where Oegerle et al. (1995) found the merging component in A2319, and has a quite large radial extent from 200 to 800 kpc.
- Sector 3 has an emission slightly higher than the azimuthally average up to 1 Mpc, where a sharp transition is present reconciling the surface brightness with the azimuthally averaged value. This sector shows evidence for a non-negligible contamination from the merger.
- Sectors 4 and 5 are quite regular, with a behaviour very similar to the azimuthally-averaged profile.
- Sector 6 shows the cold front already detected in Ghizzardi et al. (2010) and located in the SE region, about 200 kpc \approx 3 arcmin from the cluster’s center.
- Sectors 7 and 8 are the most regular ones, and reproduces very well the combined surface brightness profile.

The pressure profile obtained from the deprojected SZ signal in each sector (see Fig. 14) shows clearly that this is the quantity least affected by the dynamical history of the cluster. For instance, the merging event (Oegerle et al. 1995) happening in the NW (Sector 2) with mass ratio 3:1 is well resolved in the surface brightness/density profile, but it is not evident in the pressure profile (Sector 3 has the highest values in the pressure profile, nevertheless Sectors 1 and 2 are slightly below the azimuthally average profile), suggesting that the merger induced some shocks that have already propagated through the ICM and, at least partially, thermalized, inducing a reasonably small scatter in the pressure profile at R_{200} (see Fig. 14).

From the spectral analysis, we observe that, in Sector 2, the gas temperature reaches values below the ones measured in the

azimuthally averaged profile between 300 and 800 kpc. In Sectors 1 and 3, the temperature behaves similarly, but over a narrower radial range. These radial variations can be explained by a low temperature component contaminating Sectors 1, 2 and 3 at intermediate radii. This can be associated to the accreting substructure visible in the residual map, see Figure 13, which is merging with the main cluster halo. Over the same region, corresponding to the merging component at about 500 kpc in Sector 2, we also observe an increase in the metal abundance correlated to the gas at the lower temperature.

In Fig. 14, we show the entropy profiles obtained by solving the HEE with the *backward* method (a comparison between the profiles estimated with different methods is shown in Fig. E.3). The entropy measured in Sector 2 is well below the mean value estimated in the cluster, while Sector 1 and 3 are just slightly below. This suggests that a substructure with a low-entropy gas is still accreting into the cluster’s halo, as residual of the ongoing merger.

5.1. Azimuthal scatter and clumpiness

The azimuthal scatter of the recovered thermodynamic quantities is defined at each radius r as

$$\sigma_Q(r) = \sqrt{\frac{1}{N} \sum_{i=1}^N \left(\frac{Q_i(r) - \bar{Q}_i(r)}{\bar{Q}_i(r)} \right)^2}, \quad (13)$$

with $Q = \{ n, P, T, K, M_{tot}, M_g, f_g \}$. The profiles of the azimuthal scatter are shown in Fig. 15.

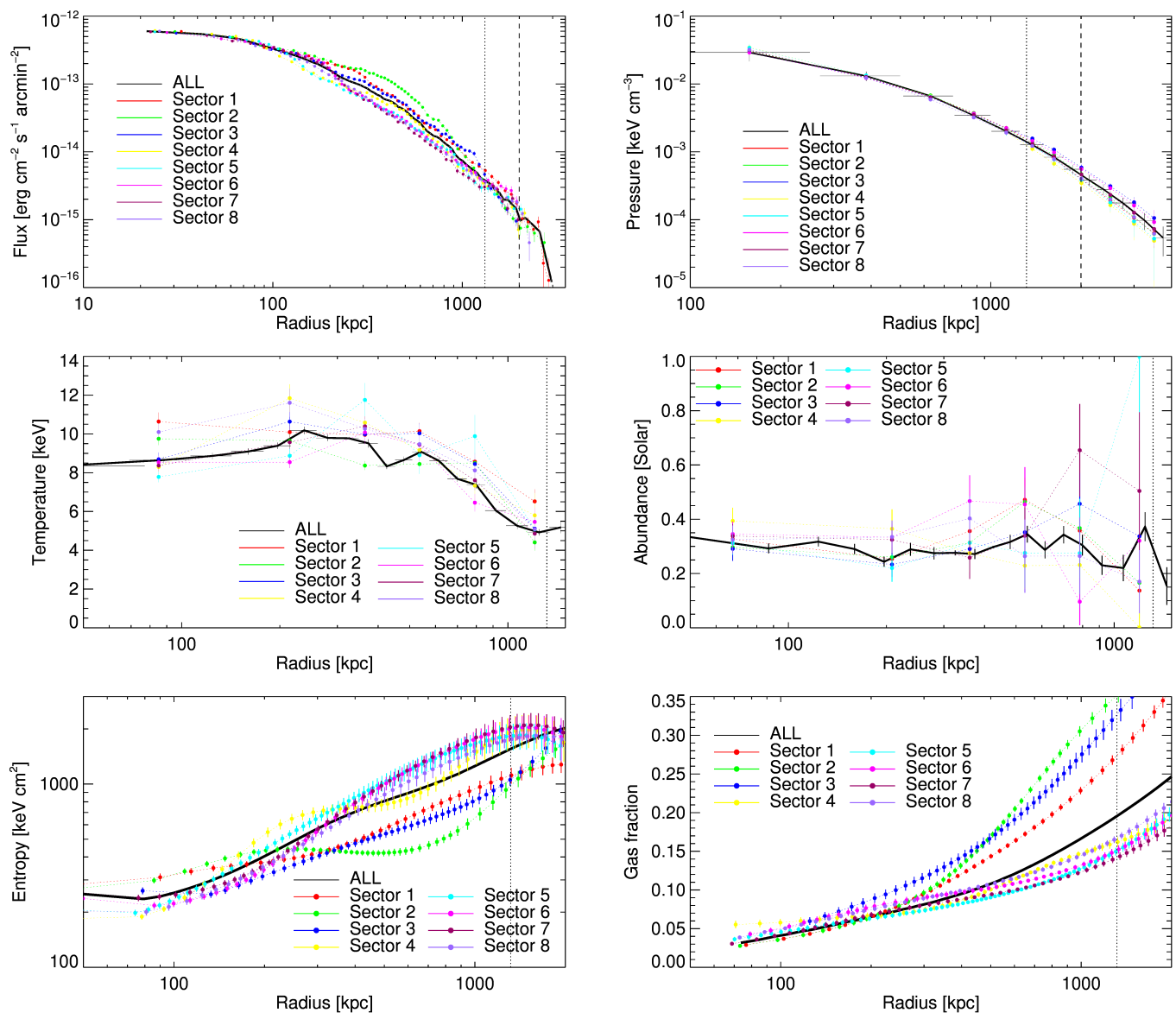


Fig. 14. (Top-Left) Surface brightness profiles for the 8 sectors using the median method. The thick black line is what we obtain in the whole image analysis. The vertical lines mark the position R_{500} and R_{200} , dotted and dashed respectively. (Top-Right) SZ pressure profiles for the 8 sectors analyzed on top of the pressure profile for the whole cluster (black line). (Center) 2D temperature (left) and abundance (right) profiles for the 8 sectors analyzed. (Bottom-Left) Reconstructed entropy profiles for all sectors using the *backward* method. The thick black line is the result for the azimuthally averaged profile. (Bottom-Right) Gas fraction profiles for the 8 sectors analyzed. The thick black line is the result for the azimuthally averaged profile. The vertical lines mark the position R_{500} and R_{200} , dotted and dashed respectively.

As a general trend, we expect that $\sigma_Q(r)$ should increase monotonously with radius, because, moving outward, the considered radial points should be less virialized. Although this is generally observed, some other features also appear. For instance, at intermediate radii (~ 600 kpc) there is a clear increase coincidentally with the clustercentric location where the merger is taking place. Moreover, there is a particular radial location between R_{500} and R_{200} , where the azimuthal scatter reaches a minimum. This point suggests the radial extension of the influence of the merger on the thermodynamic quantities.

Using this information, we can improve the characterization of the properties of the observed clumpiness in the gas density. As described in Roncarelli et al. (2013), the clumping factor of the gas (see Sect. 4.1) is expected to have two major contributors: (i) some individual clumps, (ii) large-scale accretion patterns. The latter is described by the residual clumping C_R , that,

following Roncarelli et al. (2013), can be estimated as:

$$C_R(r) = 1 + \frac{\sigma}{\sigma_0} + \frac{r}{r_0}, \quad (14)$$

where $r = R/R_{200}$; σ is the azimuthal scatter of the density n , or of the comptonization parameter y . σ_0 and r_0 are estimated from simulations (Roncarelli et al. 2013)

- $(\sigma_0, r_0) = (16.02, 5.87)$ for X-ray density
- $(\sigma_0, r_0) = (2.83, 8.25)$ for SZ comptonization parameter

We compare the estimated clumpiness with the residual clumpiness C_R in Fig. 15. We observe that the measured clumping factor, both X-ray and SZ, only slightly exceeds the estimated C_R over the entire radial range, suggesting that large-scale asymmetries account for most of the clumpiness measured.

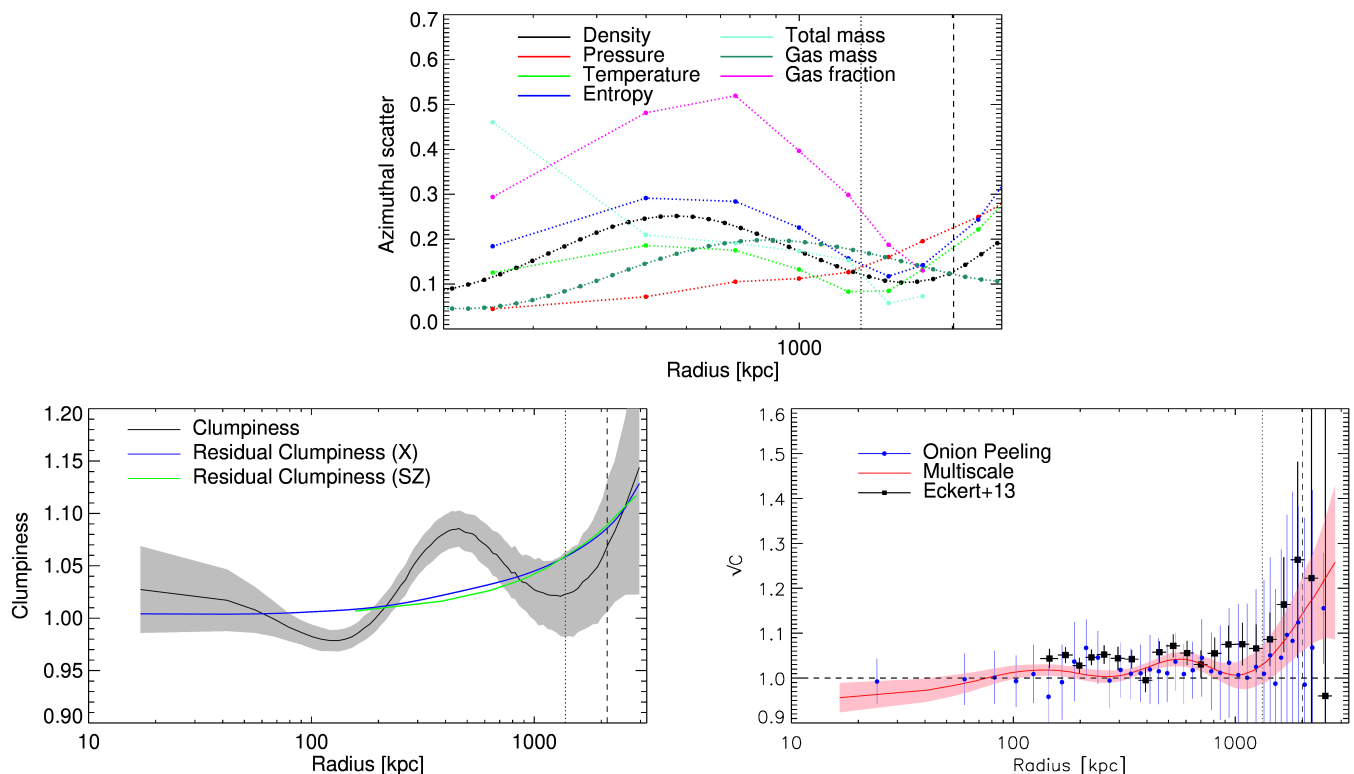


Fig. 15. (Top) Azimuthal scatter in the thermodynamic profiles: gas density and gas mass profiles are obtained from the X-ray spatial analysis; the pressure profile is the result of SZ data analysis; gas entropy and temperature are obtained by combining SZ pressure and X-ray density; the total mass is reconstructed by solving the hydrostatic equilibrium equation using the *forward* approach. The vertical dotted and dashed lines represent the location of R_{500} and R_{200} , respectively. (Center-Left) Total measured clumpiness (see Sec. 5.1; black line; shaded region represents 1 sigma uncertainty) compared with the estimated residual clumpiness using X-ray density (blue line) and SZ comptonization parameter (green line). (Center-Right) Same as Fig. 7 but removing the problematic sectors (1, 2 and 3) from the analysis. The features present in the whole clumpiness profile disappear almost completely. The vertical lines mark the position of R_{500} and R_{200} , dotted and dashed respectively. (Bottom-Left) Total measured clumpiness (see Sec. 5.1; black line; shaded region represents 1 sigma uncertainty) compared with the estimated residual clumpiness using X-ray density (blue line) and SZ comptonization parameter (green line). (Bottom-Right) Same as Fig. 7 but removing the merging region in the problematic sectors (1, 2 and 3) from the analysis. The features present in the whole clumpiness profile disappear almost completely. The vertical lines mark the position of R_{500} and R_{200} , dotted and dashed respectively.

Moreover, the clumpiness profile in Fig. 7 shows a clear excess at intermediate radii. We interpret this excess as the presence of the merger component in the NW direction. We evaluate again the clumpiness, after masking out Sectors 1, 2, and 3 more affected by the presence of the merger. As we show in Fig. 15, the excess in the clumping factor at intermediate radii disappears and the total clumpiness at R_{200} decreases to 1.05.

6. Characterizing the hydrostatic bias

6.1. Gas mass fraction and the non-thermal contribution

Since galaxy clusters originate from large regions of the primordial Universe, their baryon fraction is expected to be close to the universal fraction.

The gas mass fraction, $f_g = M_g/M_{tot}$, in massive galaxy clusters represents most of the baryons accreted in the dark matter halo and is a good proxy of the cosmic baryonic budget, which enables us to use galaxy clusters as a cosmological probe (e.g. Ettori et al. 2002, 2009).

$$\frac{\Omega_b}{\Omega_m} \cdot b = f_g + f_{star} \quad (15)$$

where Ω_b and Ω_m are the cosmological baryon and matter density, b is the depletion factor that accounts for the cosmic baryons

which thermalize in the cluster's potential, and f_{star} is the stellar mass fraction. Here, we adopt the cosmological parameters estimated from the *Planck* collaboration, $\Omega_b = 0.045$ and $\Omega_m = 0.3089$ (Planck Collaboration et al. 2016c), we assume from numerical simulations (e.g. Planelles et al. 2013) $b = 0.85$ and 0.87 (with a standard deviation of 0.03) at R_{500} and R_{200} , respectively, and consider $M_{star}/M_{gas} = 0.069$ from optical measurements in nearby systems (Gonzalez et al. 2013). We predict, thus, a gas mass fraction f_g of 0.125 and 0.128 at R_{500} and R_{200} , respectively.

However, we measure a gas fraction, already corrected for the resolved gas clumpiness using the median profile, that reaches values well above the expected f_g at $r > R_{500}$ (see Fig. 14 and 15). We advocate the role of the non-thermal pressure contribution to the estimate of the total mass in lowering the measured gas fraction.

Indeed, Abell 2319 is in a merging state (Oegerle et al. 1995), with the presence of a giant radio halo (Farnsworth et al. 2013; Storm et al. 2015) that supports this scenario. The measured gas fraction can be then biased high as a consequence of the phenomena (like gas turbulence and bulk motion) that occur during a merger and that are not accounted for in the calculation of the hydrostatic mass, causing an underestimate of the halo mass.

Before proceeding in quantifying the amount of non-thermal pressure support, we note, from the analysis in azimuthal sec-

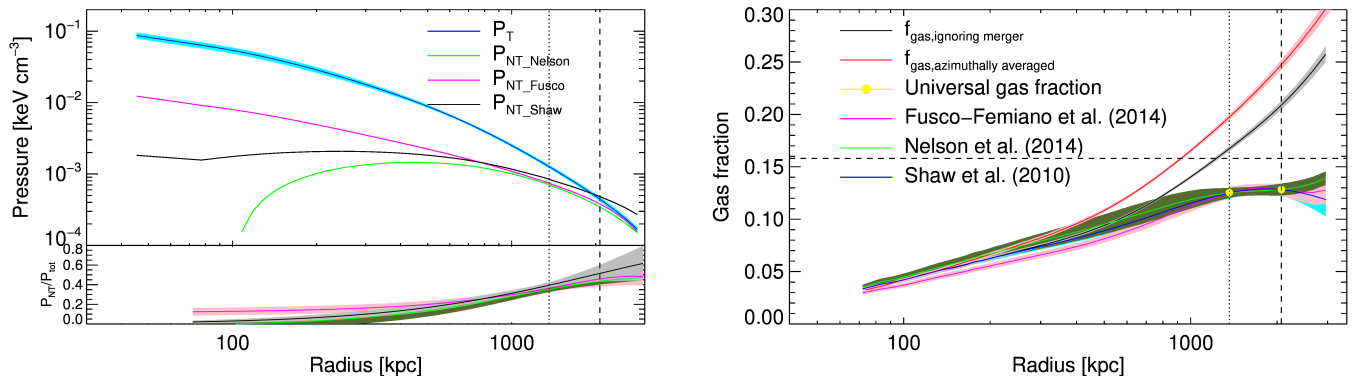


Fig. 16. (Left) Thermal pressure compared with non-thermal pressure using three different models (black, pink, and green lines, Shaw et al. 2010; Fusco-Femiano & Lapi 2014; Nelson et al. 2014, respectively). (Right) Measured gas fraction profile azimuthally averaged (red line) and ignoring the merging region (black line), and corrected accounting for the contribution of a non-thermal pressure component enabling to match the cosmic gas fraction at R_{200} and R_{500} . The horizontal line represents the “universal” baryon fraction (Planck Collaboration et al. 2016c), the vertical lines represents the position of R_{500} and R_{200} , and the yellow points are the universal baryon fraction depleted by the thermalized gas and by the star fraction. The pink, green and blue line represent the gas fraction we get by using different functional form in order to reduce the observed gas mass fraction to the universal one.

tors, that the substructure that is merging with the main halo is also able to disturb the system on a much larger scale, by enhancing the measured surface brightness up to ~ 1 Mpc. The net effect is to increase the gas mass by about 10% and so the relative amount of non thermal pressure in the outskirts. To obtain an estimate of the contribution of the non-thermal pressure unbiased from any evident merger, we ignore the region where we measure this excess in the surface brightness (see red sector in Figure 13), and repeat our analysis. We show the comparison between the results obtained before and after masking the merging region in Table 6. The hydrostatic mass remains unchanged, but the gas mass decreases, implying that the gas fraction lowers by 17% at R_{200} , but it is still larger than the cosmological gas fraction predicted from numerical simulations at these radii. We remark that the reconstructed gas fraction is already corrected for the resolved gas clumping using the median density profile, therefore clumpiness cannot be responsible for the excess gas fraction (Simionescu et al. 2011).

One possibility to explain this overestimate in the gas fraction is the presence of a substantial non-thermal pressure component in the HEE which breaks the hydrostatic equilibrium assumption. We modify the HEE in Equation 6, by adding an extra pressure component, that we define as “non-thermal” pressure and justify as generated by e.g. unresolved gas turbulence, bulk motion, magnetic field, or asphericity. This non-thermal component can be modelled, in first approximation, as a constant fraction of the thermal one (Loeb & Mao 1994; Zappacosta et al. 2006). We add this non-thermal pressure term (indicated with the subscript “NT”) in the HEE as $P_{NT}(r) = \alpha(r)P_T(r)$, where the thermal component has the subscript “T”, and $\alpha(r)$ is a function of radius. The HEE is then modified as

$$\frac{1}{\rho_g} \left(\frac{dP_T}{dr} + \frac{dP_{NT}}{dr} \right) = -\frac{G}{r^2} (M_T + M_{NT}). \quad (16)$$

and by substituting the non-thermal part we get

By solving the derivatives and readjusting the terms in the equation, we can then write how this propagates into the estimate

of the gas mass fraction:

$$\begin{aligned} f_g &= \frac{M_g}{M_T + M_{NT}} = \frac{M_g}{M_T \left(1 + \frac{M_{NT}}{M_T} \right)} \\ &= \frac{f_{g,T}}{1 + \alpha(r) - \frac{P_{NT} r^2}{GM_T \mu m_p n_e} \frac{d\alpha}{dr}} \equiv \beta f_{g,T} \end{aligned} \quad (17)$$

with β defined as the ratio between the true gas fraction and the measured thermal gas fraction. This means that in the case of $\alpha = \text{constant}$, the real gas fraction is reduced by a factor $1 + \alpha$.

By imposing that the observed cluster gas fraction should match the cosmic value in Eq. (15), and assuming a constant α , we require $\alpha = 0.64$ (0.32) at R_{200} (R_{500}), implying that about 39% (24%) of the total pressure is in the form of a non thermal component.

In general, α is expected to have a radial dependence. Numerical simulations (e.g. Shaw et al. 2010; Fusco-Femiano & Lapi 2014; Nelson et al. 2014) predict some functional forms for P_{NT}/P_T . We can constrain the parameters of these models by requiring that, if we consider the radial dependence of α in HEE, we are able to reproduce the expected gas mass fraction at R_{500} and R_{200} . The errors on the parameters are calculated using Monte Carlo simulations propagating the errors on the gas mass fraction profile, on the measure of R_{200} , and on the predicted gas mass fraction points. The non-thermal pressure profiles, and the corresponding gas fraction profiles, obtained using the above mentioned models are shown in Fig. 16, and in Table 7 we provide the three functional form adopted and the best fitting parameters. We observe that already above 200-300 kpc, the non-thermal pressure support plays a very important role in flattening the gas mass fraction profile.

Finally, by imposing that the total cluster mass M_{tot} is provided from $M_T + M_{NT}$, we can estimate the amount of the hydrostatic bias factor β as

$$\beta = \frac{M_T}{M_{tot}} \Rightarrow M_{tot} = \frac{M_T}{\beta}. \quad (18)$$

Applying Equations (16), (17) and (18), the cosmological gas fraction at R_{500} and R_{200} is obtained by requiring

$$M_{500,tot} = 10.2 \pm 0.4^{\text{stat.}} \pm 0.4^{\text{syst.}} \times 10^{14} M_{\odot}$$

Region	M_{200} ($10^{14} M_{\odot}$)	R_{200} (kpc)	$M_{gas,200}$ ($10^{14} M_{\odot}$)	$f_{gas,200}$
Azimuthally average	10.7 ± 0.5	2077 ± 33	2.54 ± 0.05	0.237 ± 0.012
Ignoring the merging region	10.7 ± 0.3	2075 ± 17	2.22 ± 0.02	0.207 ± 0.006

Table 6. Comparison between the mass reconstruction at R_{200} using the whole surface brightness image and ignoring the merging component. The columns show: the hydrostatic mass by solving HEE (see Eq. (6)), R_{200} , the gas mass obtained by integrating the gas density profile (Eq. (5)), and the gas mass fraction defined by $f_{gas} = M_{gas}/M_{tot}$.

Model	Functional form for $\alpha = P_{NT}/P_T$	a	b	c
Nelson et al. (2014)	$\left[a \left(1 + \exp \left(- \left(\frac{R}{R_{200} b} \right)^c \right) \right) \right]^{-1} - 1$	0.52 ± 0.02	0.52 (fix)	1.23 ± 0.27
Fusco-Femiano & Lapi (2014)	$a \exp \left(- \left(\frac{1-R/(2R_{500})}{b} \right)^2 \right)$	0.91 ± 0.18	0.706 ± 0.09	–
Shaw et al. (2010)	$a \left(\frac{R}{R_{500}} \right)^b$	0.63 ± 0.05	1.17 ± 0.36	–

Table 7. Model, functional form, and best fitting parameters for the three models which describe the ratio between non-thermal and thermal pressure support.

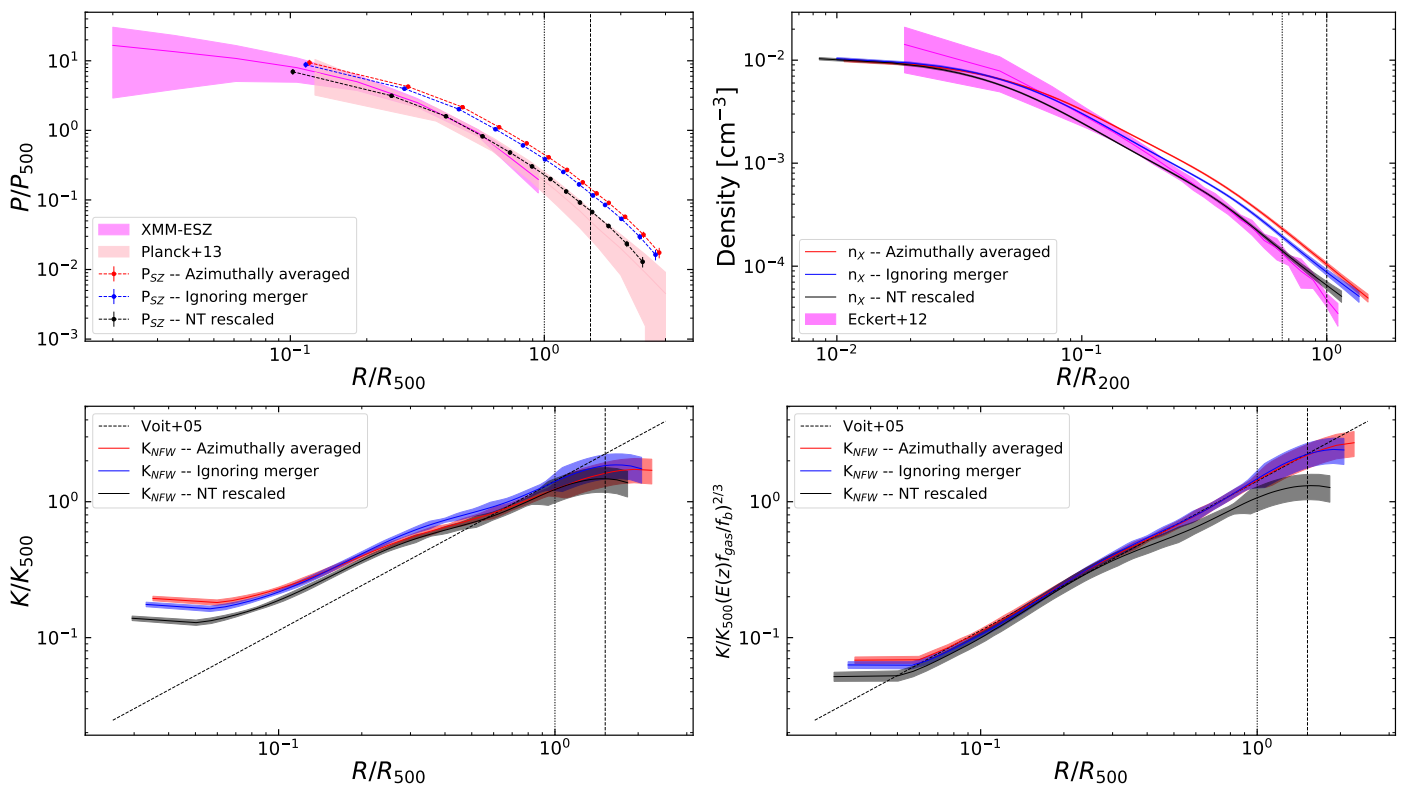


Fig. 17. Rescaled pressure (Top-left) and density (Top-right) profiles considering the azimuthally averaged, ignoring the merger, and ignoring the merging region and consider the $M_{200,tot}$ and $R_{200,tot}$ required to recover the cosmological gas fraction at the virial radius. We compare these profiles with the *Planck* envelope (Planck Collaboration et al. 2013), for pressure, and with the universal density profile (Eckert et al. 2012), for density. (Bottom) Rescaled entropy and rescaled entropy corrected by the gas mass fraction, before and after correcting for the true total mass.

$$M_{200,tot} = 17.3 \pm 0.9^{\text{stat.}} \pm 1.2^{\text{sys.}} \times 10^{14} M_{\odot}$$

Using this mass estimate corrected both by clumpiness and hydrostatic bias, and the value acquired from the *Planck* catalog (Planck Collaboration et al. 2016b) and based on scaling relations, $M_{Y_{SZ},500} = 8.74(\pm 0.12) \times 10^{14} M_{\odot}$, we infer a *Planck* bias of $1 - b = M_{Y_{SZ},500}/M_{500,tot} \approx 0.86$.

6.1.1. Effects of the hydrostatic bias on the rescaled profiles

The correction on the mass propagates to the rescale profiles, both directly since R_{500} increases shrinking the x-axis, and indi-

rectly since pressure and entropy, as described from Eq. (8) and (10) respectively, follow a rescaling which is mass dependent.

In Fig. 17, we show the net effect on the thermodynamic rescaled profiles, that can be summarized in the following statements:

- the gas pressure profile is now in agreement both with the universal pressure profile (Arnaud et al. 2010) and with the *Planck* envelope (Planck Collaboration et al. 2013);
- the gas density profile becomes compatible with the stacked density profile presented in Eckert et al. (2012);
- the gas entropy profile shows the least modification before and after this analysis; the profile becomes slightly steeper,

however it is still flat in the outskirts, in agreement with the expected impact of any non-thermal pressure support (Walker et al. 2012).

Pratt et al. (2010) have shown that in order to reconcile entropy profile with predictions from non-radiative simulations (Voit et al. 2005), the profile has to be corrected by the gas mass fraction $K \Rightarrow K \cdot (E(z)f_{gas}/f_b)^{2/3}$. Introducing this correction in each entropy profile we consider (i.e. the azimuthally average profile, the profile ignoring the merging region, and the profile required to recover the cosmological gas fraction at R_{200}), we obtain the results shown in Fig. 17. We observe that only when we include the contribution by the non-thermal pressure we obtain a corrected entropy profile that deviates from the numerical predictions, with a flattening above $0.3R_{500}$ suggesting that turbulence, or non thermal energy at large, has not been yet converted efficiently in heat energy, not allowing the specific entropy of the ICM to rise to the value expected in systems simulated in the absence of non-gravitational processes (e.g. Voit et al. 2005).

7. Summary and conclusions

The very accurate background modeling of the *XMM-Newton* exposures, and the large extension of the SZ signal resolved with *Planck* allow to combine X-ray and SZ data to study the thermodynamic properties of Abell 2319 over the virial region around R_{200} . Moreover, since the data quality is very high, we are able to study the properties of this cluster reaching the virial radius in 8 different sectors. This enables us to study the azimuthal variance of the thermodynamic properties of the ICM in this merging system for the first time.

The measured clumpiness shows the presence of the merging component with an increase in its value at intermediate radii (~ 500 kpc). This excess disappears when we remove the merging regions from the analysis. On the other hand, in the outskirts, the clumpiness measured is compatible with the estimated residual clumpiness (Roncarelli et al. 2013). This means that this cluster has no significative infalling clumps at the virial radius.

The gas density profile corrected for the resolved clumpiness is then used to recover other fundamental quantities (Eckert et al. 2015), together with the gas temperature profile that we measure, from the X-ray spectroscopic analysis, with a median relative statistical uncertainty of 2 per cent and with a systematic error that we carefully estimate to be in the order of (median value) 4 per cent, and above 15% in the outermost radial bin only. The exquisite quality of these complementary X-ray and SZ datasets, extending across R_{200} , enable us to constrain a NFW hydrostatic mass profile at very high precision ($M_{200} = 10.7 \pm 0.5^{\text{stat}} \pm 0.9^{\text{syst}} \times 10^{14} M_{\odot}$), achieving a level where systematic errors dominate over the statistical ones.

Due to the merging state of this cluster, the recovered entropy profile is flatter than the predicted one by non-radiative simulations (Voit et al. 2005). We observe the most deviations in the first and last few points: in the center this is caused by the fact that this cluster is a well known non cool core cluster (Cavagnolo et al. 2009) with a flat entropy core of ~ 75 keV cm², while some residual non-thermal energy flattens the entropy in the outskirts (Walker et al. 2012).

The pressure profile recovered from SZ data is flatter, and above the 1σ envelope, than the “universal” one measured for an ensemble of objects resolved with *Planck* (Planck Collaboration et al. 2013).

The measured gas fraction, corrected by the gas clumpiness using the median density profile, is above the value predicted from state-of-art hydrodynamical simulations for the preferred cosmological background (Planck Collaboration et al. 2016c; Planelles et al. 2013; Gonzalez et al. 2013). Analyzing the azimuthal variation of the f_{gas} profile (see Fig. 14), we observe that it is above the average value only in the sectors most affected by the merger (i.e. Sectors 1, 2 and 3). When the region with the ongoing merger and with an estimated higher gas mass is excluded from the analysis, the gas fraction drops but is still higher than the expectations, indicating a non negligible contribution from a non-thermal pressure support that we quantify in the order of 39% and 24% of the total pressure at R_{200} and R_{500} , respectively.

Once the correction induced by the non-thermal pressure support is propagated through the measurements of R_{500} , K_{500} , and P_{500} , we show that: (i) the pressure profile matches the mean behaviour of objects resolved with *Planck*; (ii) the gas density profile becomes consistent with the stacked profile obtained from Rosat/PSPC observations in Eckert et al. (2012); (iii) on the contrary, the entropy undergoes a very small change, remaining flatter than the predicted profile.

In forthcoming works, the detailed analysis presented here for A2319 will be extended to the whole X-COP sample (Eckert et al. 2017), providing the first ensembled properties of the ICM at R_{200} and above.

Acknowledgements. This research has received funding from the European Union’s Horizon 2020 Programme under AHEAD project (grant agreement n. 654215). SE acknowledges the financial support from contracts ASI-INAF I/009/10/0, NARO15 ASI-INAF I/037/12/0 and ASI 2015-046-R.0.

References

- Ameglio, S., Borgani, S., Pierpaoli, E., & Dolag, K. 2007, MNRAS, 382, 397
- Arnaud, K. A. 1996, in Astronomical Society of the Pacific Conference Series, Vol. 101, Astronomical Data Analysis Software and Systems V, ed. G. H. Jacoby & J. Barnes, 17
- Arnaud, M., Pratt, G. W., Piffaretti, R., et al. 2010, A&A, 517, A92
- Battaglia, N., Bond, J. R., Pfrommer, C., & Sievers, J. L. 2012, ApJ, 758, 75
- Binney, J. & Tremaine, S. 1987, Galactic dynamics
- Bourdin, H., Mazzotta, P., Kozmany, A., Jones, C., & Vikhlinin, A. 2017, ApJ, 843, 72
- Cavagnolo, K. W., Donahue, M., Voit, G. M., & Sun, M. 2009, ApJS, 182, 12
- Croston, J. H., Arnaud, M., Pointecouteau, E., & Pratt, G. W. 2006, A&A, 459, 1007
- De Luca, A. & Molendi, S. 2004, A&A, 419, 837
- Diehl, S. & Statler, T. S. 2006, MNRAS, 368, 497
- Dolag, K., Bartelmann, M., & Lesch, H. 1999, A&A, 348, 351
- Eckert, D., Ettori, S., Coupon, J., et al. 2016, A&A, 592, A12
- Eckert, D., Ettori, S., Pointecouteau, E., et al. 2017, Astronomische Nachrichten, 338, 293
- Eckert, D., Roncarelli, M., Ettori, S., et al. 2015, MNRAS, 447, 2198
- Eckert, D., Vazza, F., Ettori, S., et al. 2012, A&A, 541, A57
- Ettori, S., De Grandi, S., & Molendi, S. 2002, A&A, 391, 841
- Ettori, S., Donnarumma, A., Pointecouteau, E., et al. 2013, Space Sci. Rev., 177, 119
- Ettori, S., Gastaldello, F., Leccardi, A., et al. 2010, A&A, 524, A68
- Ettori, S., Ghirardini, V., Eckert, D., Dubath, F., & Pointecouteau, E. 2017, MNRAS, 470, L29
- Ettori, S. & Molendi, S. 2011, Memorie della Societa Astronomica Italiana Supplementi, 17, 47
- Ettori, S., Morandi, A., Tozzi, P., et al. 2009, A&A, 501, 61
- Farnsworth, D., Rudnick, L., Brown, S., & Brunetti, G. 2013, ApJ, 779, 189
- Foreman-Mackey, D., Hogg, D. W., Lang, D., & Goodman, J. 2013, PASP, 125, 306
- Fruscione, A., McDowell, J. C., Allen, G. E., et al. 2006, 6270, 62701V
- Fusco-Femiano, R. & Lapi, A. 2014, ApJ, 783, 76
- Ghizzardi, S., Rossetti, M., & Molendi, S. 2010, A&A, 516, A32
- Gonzalez, A. H., Sivanandam, S., Zabludoff, A. I., & Zaritsky, D. 2013, ApJ, 778, 14
- Hurier, G., Macías-Pérez, J. F., & Hildebrandt, S. 2013, A&A, 558, A118

- Kalberla, P. M. W., Burton, W. B., Hartmann, D., et al. 2005, *A&A*, 440, 775
- Kriss, G. A., Cioffi, D. F., & Canizares, C. R. 1983, *ApJ*, 272, 439
- Kuntz, K. D. & Snowden, S. L. 2008, *A&A*, 478, 575
- Lamarre, J.-M., Puget, J.-L., Ade, P. A. R., et al. 2010, *A&A*, 520, A9
- Leccardi, A. & Molendi, S. 2008, *A&A*, 486, 359
- Liu, W., Chiao, M., Collier, M. R., et al. 2017, *ApJ*, 834, 33
- Loeb, A. & Mao, S. 1994, *ApJ*, 435, L109
- Mazzotta, P., Rasia, E., Moscardini, L., & Tormen, G. 2004, *MNRAS*, 354, 10
- McCammon, D., Almy, R., Apodaca, E., et al. 2002, *ApJ*, 576, 188
- Molendi, S., De Grandi, S., Fusco-Femiano, R., et al. 1999, *ApJ*, 525, L73
- Morandi, A., Etti, S., & Moscardini, L. 2007, *MNRAS*, 379, 518
- Nagai, D., Kravtsov, A. V., & Vikhlinin, A. 2007, *ApJ*, 668, 1
- Nagai, D. & Lau, E. T. 2011, *ApJ*, 731, L10
- Navarro, J. F., Frenk, C. S., & White, S. D. M. 1997, *ApJ*, 490, 493
- Nelson, K., Lau, E. T., & Nagai, D. 2014, *ApJ*, 792, 25
- Oegerle, W. R., Hill, J. M., & Fitchett, M. J. 1995, *AJ*, 110, 32
- Pfrommer, C., Springel, V., Jubelgas, M., & Ensslin, T. A. 2007, in *Astronomical Society of the Pacific Conference Series*, Vol. 379, *Cosmic Frontiers*, ed. N. Metcalfe & T. Shanks, 221
- Pierre, M., Pacaud, F., Adami, C., et al. 2016, *A&A*, 592, A1
- Planck Collaboration, Adam, R., Ade, P. A. R., et al. 2016a, *A&A*, 594, A1
- Planck Collaboration, Ade, P. A. R., Aghanim, N., et al. 2014, *A&A*, 571, A29
- Planck Collaboration, Ade, P. A. R., Aghanim, N., et al. 2013, *A&A*, 550, A131
- Planck Collaboration, Ade, P. A. R., Aghanim, N., et al. 2016b, *A&A*, 594, A27
- Planck Collaboration, Ade, P. A. R., Aghanim, N., et al. 2016c, *A&A*, 594, A13
- Planck HFI Core Team, Ade, P. A. R., Aghanim, N., et al. 2011, *A&A*, 536, A4
- Planelles, S., Borgani, S., Dolag, K., et al. 2013, *MNRAS*, 431, 1487
- Pratt, G. W., Arnaud, M., Piffaretti, R., et al. 2010, *A&A*, 511, A85
- Read, A. M., Rosen, S. R., Saxton, R. D., & Ramirez, J. 2011, *A&A*, 534, A34
- Roncarelli, M., Etti, S., Borgani, S., et al. 2013, *MNRAS*, 432, 3030
- Salvetti, D., Marelli, M., Gastaldello, F., et al. 2017, *ArXiv e-prints* [[arXiv:1705.04172](https://arxiv.org/abs/1705.04172)]
- Schellenberger, G., Reiprich, T. H., Lovisari, L., Nevalainen, J., & David, L. 2015, *A&A*, 575, A30
- Shaw, L. D., Nagai, D., Bhattacharya, S., & Lau, E. T. 2010, *ApJ*, 725, 1452
- Simionescu, A., Allen, S. W., Mantz, A., et al. 2011, *Science*, 331, 1576
- Snowden, S. L., Mushotzky, R. F., Kuntz, K. D., & Davis, D. S. 2008, *A&A*, 478, 615
- Storm, E., Jeltama, T. E., & Rudnick, L. 2015, *MNRAS*, 448, 2495
- Struble, M. F. & Rood, H. J. 1999, *ApJS*, 125, 35
- Sunyaev, R. A. & Zeldovich, Y. B. 1972, *Comments on Astrophysics and Space Physics*, 4, 173
- Tauber, J. A., Mandolesi, N., Puget, J.-L., et al. 2010, *A&A*, 520, A1
- Tchernin, C., Eckert, D., Etti, S., et al. 2016, *A&A*, 595, A42
- Tozzi, P. & Norman, C. 2001, *ApJ*, 546, 63
- Vazza, F., Eckert, D., Simionescu, A., Brügggen, M., & Etti, S. 2013, *MNRAS*, 429, 799
- Vazza, F., Roncarelli, M., Etti, S., & Dolag, K. 2011, *MNRAS*, 413, 2305
- Vikhlinin, A., Kravtsov, A., Forman, W., et al. 2006, *ApJ*, 640, 691
- Voit, G. M., Kay, S. T., & Bryan, G. L. 2005, *MNRAS*, 364, 909
- Walker, S. A., Fabian, A. C., Sanders, J. S., & George, M. R. 2012, *MNRAS*, 427, L45
- Willingale, R., Starling, R. L. C., Beardmore, A. P., Tanvir, N. R., & O'Brien, P. T. 2013, *MNRAS*, 431, 394
- Zappacosta, L., Buote, D. A., Gastaldello, F., et al. 2006, *ApJ*, 650, 777
- Zhuravleva, I., Churazov, E., Kravtsov, A., et al. 2013, *MNRAS*, 428, 3274

Appendix A: Non X-ray background modeling

We developed and calibrated a novel technique to model and subtract the non X-ray background (NXB). Our approach builds upon the method devised in Tchernin et al. (2016), however it can be more reliably applied to observations including a significant source emission above 5 keV. Here we describe the main principles of our method and validate it using a large set of blank-sky *XMM-Newton* pointings.

Appendix A.1: Model

It has long been known that the NXB of *XMM-Newton* is split into two main components, the quiescent particle background (QPB) and the soft protons (SP). Recently, Salvetti et al. (2017) analyzed almost the complete *XMM-Newton* archive and showed the presence of an additional stable, low-intensity component within the field of view (FOV) of the MOS2 instrument, whose origin is yet unknown. As described in Section 2, a fraction of the area of the MOS detectors is located outside the FOV of the *XMM-Newton* telescopes. The outFOV area can be used to estimate the QPB level in each observation by rescaling filter-wheel-closed data to the measured outFOV count rate. The remaining inFOV high-energy count rate can then be decomposed into a variable component (SP) and a quiescent part (QC). We can thus describe the remaining NXB as

$$\text{inFOV} - \text{outFOV} = \text{SP} + \text{QC} \quad (\text{A.1})$$

where inFOV and outFOV denote the [7-11.5] keV MOS2 count rates measured in the exposed and unexposed areas of the detector, respectively. We restrict the measurement to the MOS2 detector as two of the MOS1 chips have been lost throughout the mission, and the unexposed area of the pn detector is too small for our needs.

Importantly, the SP component is expected to show a different spatial signature on the detector compared to the QPB. Indeed, soft protons, which are funneled towards the detector through the telescope, are more spatially concentrated than the QPB and follow a vignetting curve $SP(r)$ that is different from the vignetting curve of the photons (Kuntz & Snowden 2008), where r denotes the distance of each pixel from the aim point. Conversely, given that its origin is currently unclear, the spatial distribution of the QC component is unknown. Here we make the hypothesis that this component is flat over the detector.

Appendix A.2: Blank-sky dataset and modeling

To determine the relative contributions of the SP and QC components, we used a large set of 495 *XMM-Newton* blank-sky pointings, most of which from the XXL survey (Pierre et al. 2016). Our dataset comprises more than 5 Ms of data. We processed the data using ESAS in the same way as for the A2319 data (see Section 2). We estimated the QPB component in each observation by measuring the outFOV count rate and rescaling filter-wheel-closed data. We also compute the high-energy inFOV and outFOV count rates for each observation. We then measured the radial profiles in the [0.7-1.2] keV band of the blank-sky pointings from the aim point to the outermost edge of the pointing in annuli of 30 arcsec width. The detected sources were masked and the QPB was subtracted from the data. As already shown in Tchernin et al. (2016), this procedure results in radial profiles that are on average not flat, which indicates the need of modeling additional components (SP and QC).

We then describe the radial profiles $S_X(r)$ as the sum of the SP and QC components following their respective spatial distributions,

$$S_X(r) = C + N_{QC} + N_{SP}(\text{inFOV} - \text{outFOV} - \bar{QC})SP(r), \quad (\text{A.2})$$

where C is the sky background intensity at the relevant location, N_{QC} the intensity of the stable QC component, N_{SP} the normalization of the variable SP, and $\bar{QC} = 0.023$ counts/s is the mean high-energy count rate of the QC component (Salvetti et al. 2017). We then perform a joint fit on all the measured profiles and optimize for the values of N_{QC} and N_{SP} . We then used the best-fit values of N_{QC} and N_{SP} to create 2D models of these components and subtract them from the data.

In Fig. A.1 we show the stacked radial profiles of the full sample. In the left-hand panel we show the stacked profiles obtained when subtracting the QPB component only, whereas in the right-hand panel, the SP and QC components have been modeled using the method described above and subtracted from the data. To investigate the dependence of our results on SP contamination, we grouped the data in bins of increasing SP contamination, which we trace using the inFOV/outFOV ratio (Leccardi & Molendi 2008). Observations that were mildly affected by SP contamination exhibit a inFOV/outFOV ratio close to one, whereas heavily contaminated observations show high values of the inFOV/outFOV ratio. The effect of SP contamination is evident in the left-hand panel of Fig. A.1, where the deviations of the stacked profiles from a straight line progressively increase with increasing SP contamination. Conversely, when applying our SP and QC modeling approach, flat profiles are found in all 4 bins out to the edge of the FOV, indicating that our model accurately reproduces the various NXB components. The excess scatter compared to a straight line is 5%, which we adopt as our systematic uncertainty in the subtraction of the NXB.

Appendix B: Results of the spectral fitting

radii arcmin	C-stat.	PHA bins	C-stat. reduced	net cts 10^3	SBR	n_H 10^{22} cm^{-2}
-	-	-	-	-	-	-
0.00 - 1.05	2746	2603	1.05	170	85	0.075
1.05 - 1.63	2698	2591	1.04	155	58	0.078
1.63 - 2.18	2748	2552	1.08	148	42	0.081
2.18 - 2.74	2773	2575	1.08	145	32	0.077
2.74 - 3.32	2767	2484	1.11	131	24	0.078
3.32 - 3.98	2688	2573	1.05	133	17	0.081
3.98 - 4.65	2807	2582	1.09	134	14	0.079
4.65 - 5.37	2912	4005	0.73	131	11	0.075
5.37 - 6.14	2666	2387	1.13	112	8.6	0.074
6.14 - 6.95	2811	2481	1.13	101	6.8	0.077
6.95 - 7.83	3157	4949	0.64	92	5.1	0.074
7.83 - 8.85	3305	3866	0.85	89	3.6	0.073
8.85 - 10.05	3697	6052	0.61	82	2.5	0.074
10.05 - 11.51	4514	3868	1.17	80	1.7	0.076
11.51 - 13.10	4870	3583	1.36	62	1.2	0.079
13.10 - 15.18	4893	3494	1.40	46	0.9	0.077
15.18 - 17.70	2808	1844	1.52	20	0.9	0.121
17.70 - 20.63	2632	2175	1.21	19	0.6	0.101
20.63 - 24.08	2098	1916	1.09	12	0.4	0.113

Table B.1. Statistical results of the fitting in the annular regions, with radial extension, C-statistic, number of spectral bins, reduced C-statistic indicated, net number of photons in the energy band [0.5-11.3] keV, signal to background ratio, and best fit n_H .

In Table B.1, we show the spectral fit results in the analysis described in Section 2, indicating the radial extension of the chosen annuli, the C-statistic, the number of the spectral bins,

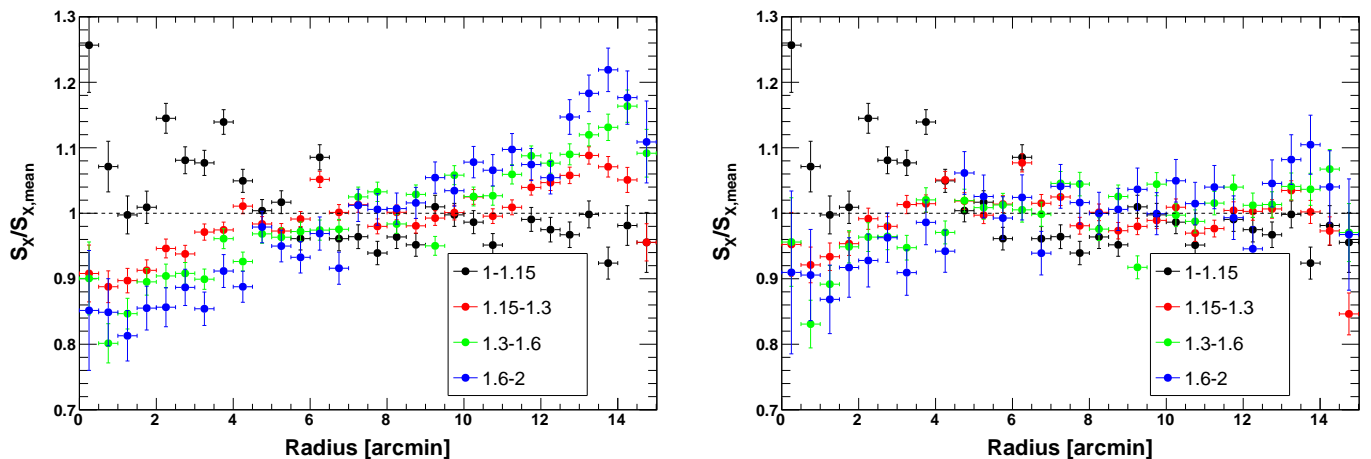


Fig. A.1. Stacked EPIC radial profiles of 495 blank-sky pointings, sorted in bins of soft-proton contamination inFOV/outFOV. The black data points show observations with low SP contamination (inFOV/outFOV=1-1.15), whereas the blue points comprise observations that were severely affected by SP contamination (inFOV/outFOV=1.6-2.0). The left-hand panel shows the stacked profiles obtained when subtracting only the QPB component, while in the right-hand panel, the SP and QC components have been taken into account following Eq. A.2.

and the reduced C-statistic. We point out that this last quantity is always order of 1, implying high goodness in the fit.

Since A2319 is located at low galactic latitude, $b = +13.5^\circ$, the choice to leave free n_H to vary is reinforced from the azimuthal variation over the cluster's region of the dust emission as mapped at $100 \mu\text{m}$ by the InfraRed Astronomical Satellite (IRAS; see Fig. B.1). The map shows that the sectors 5, 6, and 7 are the ones expected to have higher Galactic absorption. Indeed the n_H in the 8 considered sectors varies according to Table B.2, with sector 5, 6, and 7 being $\sim 10\%$ above the other sectors.

Sector	1	2	3	4	5	6	7	8
$n_H [10^{20} \text{cm}^{-2}]$	7.65	7.20	7.62	7.87	8.39	8.57	8.41	7.99

Table B.2. Best fit n_H in the 8 sectors considered.

Appendix C: Comparison with *Chandra* data

We have analyzed two archival *Chandra* observations of the inner region of A2319 (OBSID 15187, with a cleaned exposure time of 75 ksec, and OBSID 3231, with 15 ksec). We have processed the two *Chandra* ACIS-I observations of A2319 with a standard pipeline based on CIAO 4.9 (Fruscione et al. 2006) and CALDB 4.7.4 to create a new events-2 file which includes filtering for grade, status, bad pixels and time intervals for anomalous background levels. The background is estimated through blank sky observations. We have extracted the spectra in the same annular regions as for *XMM-Newton*, and fit them in the identical way, leaving the galactic column density n_H free to vary within the range $7 - 13 \times 10^{20} \text{cm}^{-2}$. The temperature profiles are compared in Fig. C.1. We observe a good agreement among these spectral measurements, despite the claimed, and still debated, cross-calibration issue between *Chandra* ACIS and *XMM-Newton* EPIC (see e.g. Schellenberger et al. 2015), in particular in very hot systems ($T > 5 \text{keV}$) as A2163. We suggest that leaving free n_H plays a determinant role in adjusting the relative impact of the soft part of the spectra, where most of the observed systematic tension has been reported. In the present case, *Chandra* prefers systematically higher values of n_H ($\sim 1.2 - 1.3 \times 10^{21} \text{cm}^{-2}$) than *XMM-Newton* (see Tab. B.1) in all the radial bins. These higher values are more in agree-

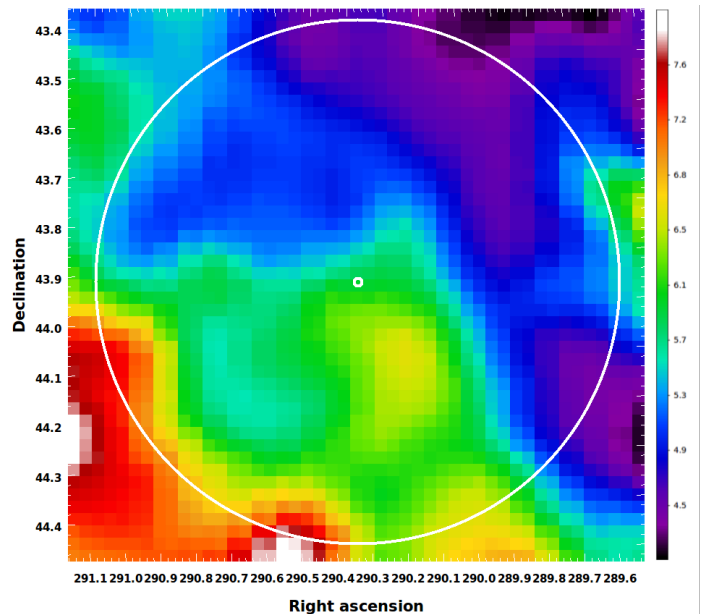


Fig. B.1. IRAS map (minimum-maximum values in the region within R_{200} are 4.22, 7.77 MJy/sr). The white external circle represents the location of R_{200} , while the small one represents the location of the center of the cluster.

ment with the column density corrected for molecular hydrogen as suggested in Willingale et al. (2013).

Appendix D: Likelihood for the mass reconstruction

We fit our thermodynamic quantities using the MCMC code *emcee* (Foreman-Mackey et al. 2013), for which we define a likelihood. We included in the fitting procedure an intrinsic scatter, which is added quadrature on the error of logarithm of pressure such that $\log P \sim \log P \pm \sigma_{int}$. By assuming a small value for σ_{int} we can write

$$\sigma_{P,int} \approx \frac{P \cdot \exp(+\sigma_{int}) - P \cdot \exp(-\sigma_{int})}{2} = P \cdot \sinh \sigma_{int}$$

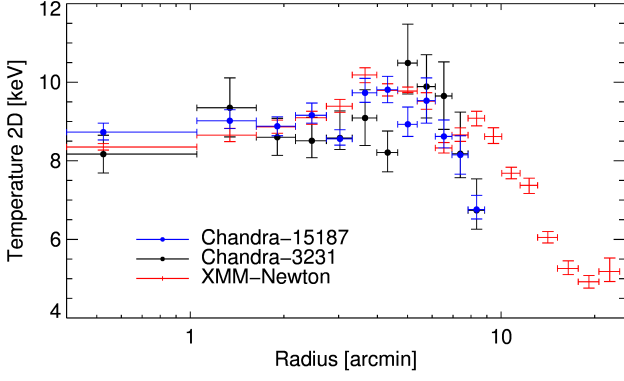


Fig. C.1. Comparison between the spectral temperature obtained using *Chandra* and *XMM-Newton*. There is a clear excess in the temperature measured by *Chandra* of the order of 2-3 keV up to 7 arcmin.

Summed to the covariance matrix as follows:

$$\Sigma_{tot} = \begin{bmatrix} \Sigma_{11} & \Sigma_{12} & \Sigma_{13} & \dots & \Sigma_{1n} \\ \Sigma_{21} & \Sigma_{22} & \Sigma_{23} & \dots & \Sigma_{2n} \\ \vdots & \vdots & \vdots & \ddots & \vdots \\ \Sigma_{n1} & \Sigma_{n2} & \Sigma_{n3} & \dots & \Sigma_{nn} \end{bmatrix} + \begin{bmatrix} \sigma_{P_{1,int}}^2 & 0 & 0 & \dots & 0 \\ 0 & \sigma_{P_{2,int}}^2 & 0 & \dots & 0 \\ \vdots & \vdots & \vdots & \ddots & \vdots \\ 0 & 0 & 0 & \dots & \sigma_{P_{n,int}}^2 \end{bmatrix}$$

where $\Sigma_{i,j}$ is the covariance matrix on the measured *Planck* pressure profile.

The intrinsic scatter is propagated also to the variance on temperature profile, added in quadrature to the measured errors:

$$\sigma_{tot}^2 = \sigma_T^2 + \sigma_{T,int}^2$$

with

$$\sigma_{T,int} = \frac{P_{model}}{n_{model}} \sigma_{P,int} = T_{model} \cdot \sigma_{P,int}$$

We remind that in general the likelihood is defined as:

$$\mathcal{L} = \frac{1}{\sqrt{2\pi\sigma^2}} \exp(-\chi^2/2)$$

so that

$$\log \mathcal{L} = -0.5(\chi^2 + \log \sigma^2 + \log(2\pi))$$

where the last term is a constant and therefore is usually ignored while maximizing the likelihood, but the term with $\log \sigma^2$ is not. Finally, by using the subscript “m” or “o” to describe model predicted or observed quantities respectively, we can explicitly write the logarithm of the likelihood we use to fit:

$$\begin{aligned} \log \mathcal{L} = & -0.5 [(P - P_m)\Sigma_{tot}^{-1}(P - P_m)^T + n \log(\det(\Sigma_{tot}))] \\ & -0.5 \sum_{i=1}^n \left[\frac{(T_i - T_{m,i})^2}{\sigma_{T,i}^2 + \sigma_{T,int}^2} + \log(\sigma_{T,i}^2 + \sigma_{T,int}^2) \right] \\ & -0.5 \left[\sum_{i=1}^n \frac{(\epsilon - \epsilon_{m,i})^2}{\sigma_{\epsilon,i}^2} \right] \end{aligned}$$

We point out that this method is independent on how P_{model} and T_{model} are computed, meaning that this kind of approach is valid both for the *forward* and *backward* methods.

Appendix E: Thermodynamic quantities in azimuthal sectors

The procedure described in Sections 2 to 4 are applied on each azimuthal sector. In summary we deproject surface brightness into density using the multiscale technique on the mean profile, we deproject comptonization parameter to retrieve pressure, and we calculate the temperature in 6 spectral annuli. We then apply the *backward* approach on these thermodynamic quantities, in order to find the parameters of a NFW mass model which best reproduce the observables. We compare the observed and reconstructed from the best-fit mass model pressure and temperature profiles sector by sector in Fig. E.1 and E.2, respectively. We observe that the only sectors with an evident discrepancy are the one disturbed the most by the merger event, i.e. Sector 1, 2 and 3.

Similarly to what has been done in Section 4.5, we compare the entropy profile reconstructed by the NFW *backward* best fit, with the entropy recovered from X-ray spectroscopy ($K = kT/n_e^{2/3}$), and with the entropy recovered by combining X-ray density and SZ pressure ($K = P/n_e^{5/3}$); this comparison sector by sector is shown in Fig. E.3.

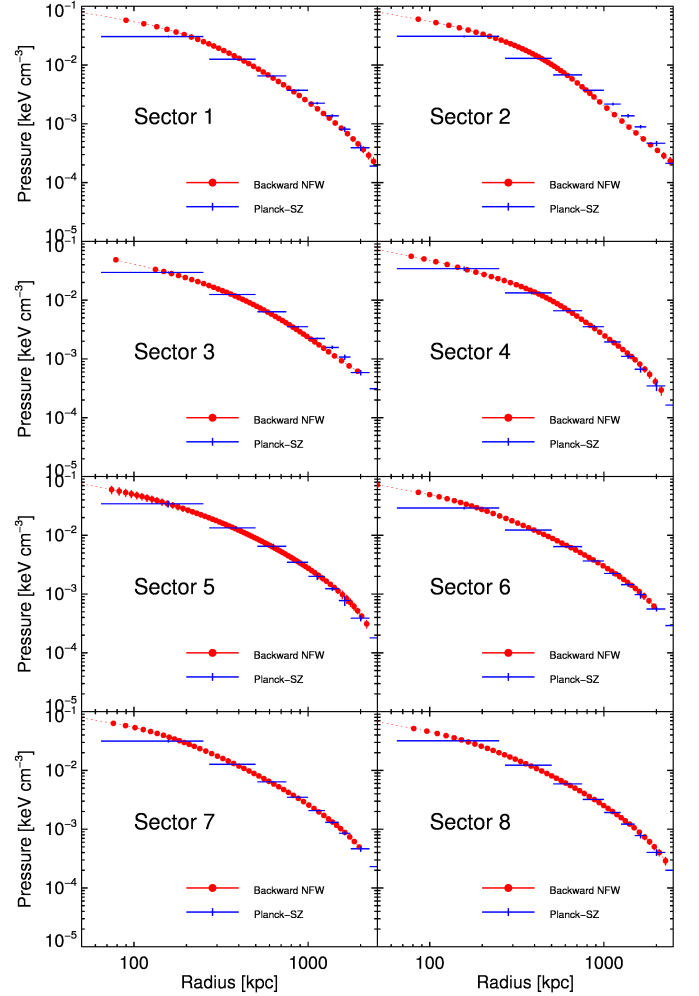


Fig. E.1. Comparison of the observed pressure profile with the one reconstructed by the NFW *backward* best fit.

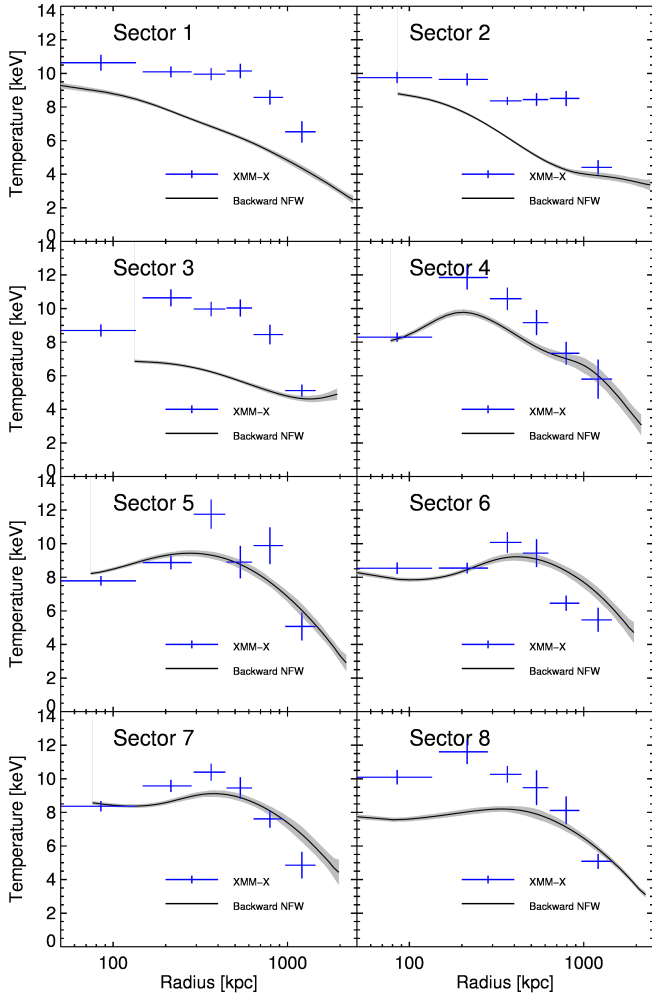


Fig. E.2. Comparison of the observed 2-dimensional temperature profile with the one reconstructed by the NFW *backward* best fit.

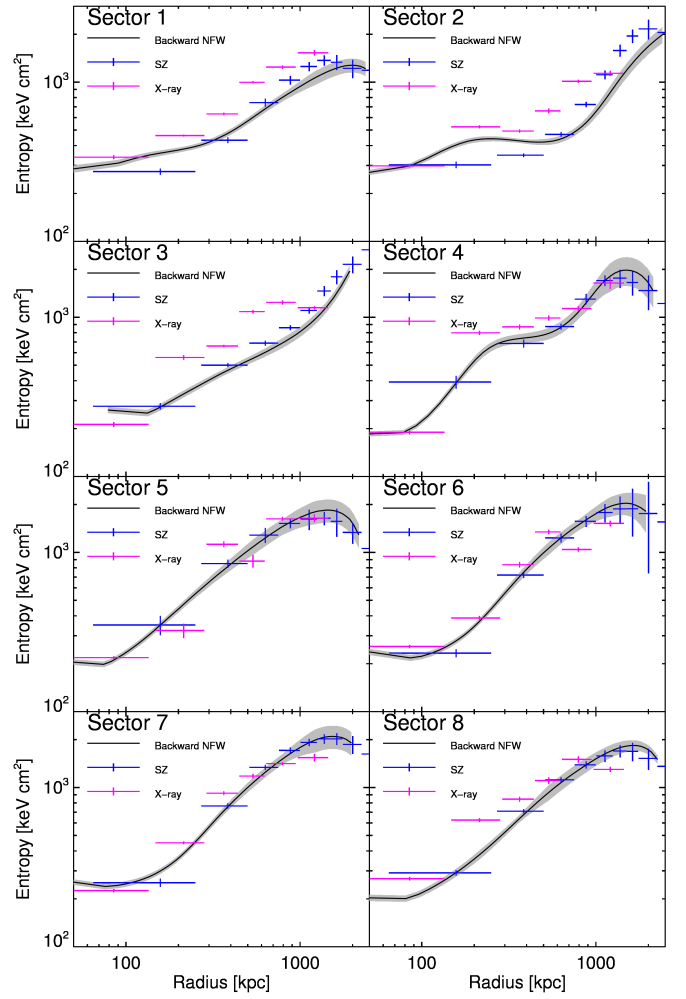


Fig. E.3. Comparison between the entropy profile reconstructed by the NFW *backward* best fit with the entropy coming from the combination of X-ray and SZ and just using X-ray spectral results.